An experimental investigation into the spread and heat transfer dynamics of a train of two concentric impinging droplets over a heated surface

Ganesh Guggilla[1], Ramesh Narayanaswamy[2], Arvind Pattamatta*

Abstract

Extensive studies of two concentric droplets consecutively impinging over a thin heated foil surface are carried out to compare the spread and heat transfer dynamics of a single drop, and drop-on-drop configurations using high speed imaging and infrared thermography. Millimeter-sized deionized water droplets (2.80 ± 0.04 mm) are impinged upon a heated Inconel surface (thickness of 25 μm) from a fixed height corresponding to a Weber number (We) of 50 ± 2 and Reynolds number (Re) of 3180 ± 90 with a flow rate of 20 droplets per minute. Surface temperature is chosen as a parameter, and is varied from 22 °C (non-heated) to 175 °C. Temperature and heat flux distributions associated with droplet-surface interactions are obtained, and the outcomes of the process are measured in terms of spread diameter, droplet input heat transfer, dynamic contact angle, and surface mean temperature. A decline in the droplet heat transfer for drop-on-drop impingement is observed for all temperatures investigated in the present work. This is attributed to the surface pre-cooling by the initial droplet and also to the reduced surface area-to-volume ratio i.e., increased spreading film thickness. High heat transfer rates are observed around the three-phase contact line region, especially during the receding phase of the droplet, for both configurations, confirming the significance of contact line evaporation in droplet-hot wall interactions. Theoretical models predicting the maximum spread factor and corresponding input heat transfer into the droplet are identified from the literature, and found to be in good agreement with present experimental observations.

Keywords: spread dynamics, droplet heat transfer, concentric droplet impact, drop-on-drop

*Associate Professor, IIT Madras, India
Email address: arvindp@iitm.ac.in (Arvind Pattamatta)
[1]Joint doctoral scholar , IIT Madras - Curtin University
[2]Associate Professor, Curtin University, Australia

1. Introduction

Various natural and industrial processes requires the knowledge of droplet interactions with surfaces. The underlying physics of these droplet systems is complex, and has triggered many experimental and numerical investigations in the past decades. Applications such as ink jet printing, spray coating, and tablet encapsulation requires the study of droplet dynamics over adiabatic (non-heated) surfaces. Droplet interaction with heated walls is the topic of interest in processes such as metal quenching, spray cooling, fuel-air interaction in internal combustion engines, power plant engineering and refrigeration.

From earlier studies conducted on droplet impingement over adiabatic surfaces, the droplet impact scenario can be classified into three types based on the nature of target, i.e., solid wall, liquid film and deep liquid pool. Extensive reviews on these subtopics have been provided by Prosperetti and Oguz [1], Rein [2] , Yarin [3], Marengo et al. [4], Moreira et al. [5], and Josserand and Thoroddsen [6]. They have summarized several aspects associated with the hydrodynamics of the impingement process i.e., nature of impact, surface wettability, influence of thermophysical properties, and the observed regimes of evaporation.

In the case of droplet impingement over hot surfaces, the process involves mass, momentum and heat transfer interactions, and thereby requires additional efforts for better understanding of the phenomenon. A comprehensive review of studies concerning the fluid mechanics and heat transfer mechanisms of liquid drop impact on a heated wall is presented by Liang and Mudawar [7]. Significant contributions were made in the literature in understanding the interfacial behaviour of droplet from the moment of impact over heated surfaces. It has been observed that heat transfer in droplet impingement over a hot surface is strongly dependent on the magnitude of wall temperature relative to the liquid's saturation temperature. Factors such as droplet diameter, impact velocity, physical properties of the liquid, nature of the surrounding gas, and wall characteristics can also influence the overall process. Four distinct regimes were identified based on the evaporation lifetime of a single drop at different wall temperatures as film evaporation, nucleate boiling, transition boiling and film boiling [8, 9]. Efforts were made to quantify the impact dynamics and heat transfer behaviour in those regimes in order to characterize the droplet-hot wall interactions. Bernardin et al. [10, 11] revealed that wall temperature and impact Weber number are the

two most influencing parameters governing the impingement process over heated surfaces. Impingement studies were carried out for low and high Weber numbers and extensive maps concerning the impact and heat transfer were provided. They have also studied the effect of surface roughness and found that surface features can influence the observed boiling regimes. Using advanced diagnostic tools such as high speed imaging [12–14], interferometry and total internal reflection techniques [15, 16], attempts were made to quantify the droplet boiling regimes based on the observations of hydrodynamic behaviour during impact.

Film evaporation takes place when the wall temperature is below the liquid's saturation temperature, and even when the wall is superheated but insufficient to initiate bubble nucleation inside the drop upon contact with the surface [7]. It is observed that, in film evaporation regime, droplet heat transfer is affected by temperature variations inside the droplet, wall heat flux and droplet evaporation rate [17–21]. Chandra et al.[22] investigated the effect of contact angle on droplet evaporation rate by experimental investigation. They have used a surfactant to reduce the contact angle resulting in higher evaporation rates. Pasandideh-Fard et al.[23] presented a numerical model and carried out simulations revealing that impact velocity has a minor influence on the overall droplet heat transfer. From these works, it is identified that wall temperature is lowest at the impact point and increase in the radial direction toward the edge of the droplet. Investigators [24, 25] also found that the evaporation rate is highest at the three-phase contact line and several numerical predictions [17, 20, 26–30] have confirmed these observations.

Nucleate boiling regime is the region extended from the point of bubble nucleation, which will take place when wall temperature is above the saturation temperature, to the critical heat flux point which corresponds to shortest droplet evaporation time. Tarrozzi et al.[31] demonstrated a non-intrusive optical method to measure liquid-solid contact temperature where an infrared camera was used to capture the foot print from the underside of the impact surface. It was reported that the onset of the nucleate boiling depends on contact temperature, and observed the regime when contact temperature exceeds the liquid's saturation temperature. Studies on the effect of the dissolved gases and salts [24], surface thickness [25], surfactants [32], nano fluids [33], droplet size and physical properties [34] on the incipience of bubble nucleation are available. Predictions of critical heat flux temper-

atures [10, 11, 35] were also reported in the literature for different liquids including water, and correlations provided [36, 37] for corresponding maximum heat transfer rate.

For liquid-solid interface temperatures at or above certain temperature, named as the Leidenfrost temperature, the liquid in the immediate vicinity of the wall is instantaneously converted to vapour upon contact, and forms a continuous insulating vapour layer between the liquid and the wall [38, 39]. In literature, this temperature is identified as the lowest wall temperature of the film boiling regime and has been studied in relation to sessile drop over hot surface termed as static Leidenfrost temperature [12, 33, 40]. While, for impinging droplets, this temperature is termed as dynamic Leidenfrost temperature where rebound of the droplet from the surface can be observed [33, 39, 41]. Influence of pressure, wall roughness, gravity and surface tension on static Leidenfrost temperature [40, 42–44], and correlations [45, 46] concerning the precise prediction of dynamic Leidenfrost temperatures in terms of saturation temperature, static Leidenfrost temperature and impact Weber number are also available. In a recent work [47, 48], it is shown that microscale droplets with low impacting velocities can find themselves in a Leidenfrost-type regime (levitating over the substrate) at substrate temperatures not only far below the Leidenfrost temperature but even below the saturation temperature. In addition, using levitating microdroplets as tracers it is shown that evaporation rate has a maximum at the three-phase contact line, confirming the results of other studies [24, 25].

The above described studies are related to a single droplet impingement over a hot target surface. Consequently, in order to understand the cooling mechanisms such as spray cooling, basic processes such as drop-on-drop impact and multiple droplet interference have to be studied. Bernardin and Mudawar [49] presented an empirical approach to determine film boiling heat transfer of a spray from extrapolation of the heat transfer characteristics of an isolated droplet stream. They found that interference resulting from a drop impinging on top of another spreading drop or with an offset between the droplets, minimizes effective liquid-solid contact area and corresponding heat transfer rate, in contrast to isolated drops. Fujimoto et al.[50] studied the successive impact of drops over heated surfaces and presented the discussion of hydrodynamics for both normal and oblique impacts on the walls. Breitenbach et al.[51] developed a model for heat transfer rate into a single drop impacting onto

a hot solid wall and then used it to estimate the an average heat transfer coefficient for spray cooling in the film boiling regime. Minamikawa et al.[52] numerically studied successive impact of two drops on a heated wall and found that the morphology in film boiling regime is strongly dependent on vertical spacing between the drops. Guggilla et al.[53] used a phase-change numerical model and studied the drop-on-drop impact over heated surfaces in film evaporation regime. The effect of non-dimensional numbers on evaporation dynamics of drop-on-drop collision and theoretical model to evaluate the numerical findings was developed. Batzdorf et al.[54] developed a numerical model and simulated simultaneous collisions of two drops with a solid substrate.

From the previous studies, it can be observed that the impact dynamics and heat transfer mechanism involved in multiple droplet collisions are not fully known. There is a need to assess various configurations of these droplet collisions and its interference over heated surfaces for different boiling regimes. Comparison with an isolated droplet impact and theoretical models estimating the dynamics of the process will provide more insights in understanding the physical process of spray cooling. The present work is aimed at studying the spread and heat transfer dynamics of a consecutive impingement train of two water droplets. High-speed photography and infrared thermographic techniques are employed to capture the post impingement events associated with the process.

A thin Inconel 600 foil has been used as the target surface and temperature is chosen as the parameter, varied from ambient temperature of 22 °C to 175 °C, and found to be within the film evaporation regime. From the instant of impact, the droplets are found to undertake a series of spreading and receding phases until it achieves an equilibrium and evaporates as a spherical liquid cap [7]. In the present work, the impact dynamics of droplet initial stage i.e., spreading and receding phases are captured and studied in detail. The event of consecutive impact is considered as two separate configurations i.e., single droplet and drop-on-drop impact. The temporal variation of droplet deformation in terms of spread diameter, dynamic contact angle and heat transfer rate are used and compared for these configurations.

Nomenclature

A_e	Effective area, m^2
A_e^*	Dimensionless effective area
c	Specific heat capacity of the heater, J/kgK
d	Instantaneous spread diameter, mm
DPM	droplets per minute
D	Impacting droplet diameter, mm
D_s	Sessile droplet diameter, mm
g	Acceleration due to gravity, m/s^2
h_s	height of the sessile droplet, mm
h_{max}	height of the droplet at maximum spread, mm
h_{lv}	Latent heat of vaporization, J/kg
m	Mass of liquid droplet, kg
NETD	Noise Equivalent Temperature Difference
Q_{cond}	Net conduction heat transfer, W
Q_{conv}	Convective heat transfer, W
Q_{drop}	Droplet input heat transfer, W
Q_{gen}	Generated heat, W
Q_{rad}	Radiation heat transfer, W
Q_{stored}	Stored heat, W
Q^*	Effectiveness or cooling efficiency
Q_e^*	Dimensionless evaporation heat transfer (mass)
S^*	Spread factor, (d/D)
S_{max}^*	Maximum spread factor, (d_{max}/D)
T	Temperature of the surface, $^\circ C$
T^*	Dimensionless temperature
t	Time, ms
dt	Time interval, ms
T_∞	Ambient temperature, $^\circ C$
T_{sat}	Saturation temperature, $^\circ C$

U	Impact velocity of droplet, m/s
V	Volume of the droplet, m^3

Non-dimensional quantities

Bo	Bond number, $\rho_l g D^2/4\sigma$
Ja	Jakob number, $c\Delta T/h_{lv}$
Pr	Prandtl number, $\mu_l c_{p_l}/k_l$
Re	Reynolds number, $\rho_l U D/\mu_l$
We	Weber number, $\rho_l D U^2/\sigma$

Greek letters

ϵ	Effectiveness ratio
θ	Three-phase contact angle, degree
σ_{sd}	Standard deviation
τ	Non-dimensional time, tU/D

Subscripts

f	final
i	initial
l	liquid
max	maximum

2. Experimental methodology

Experimental apparatus consists of image acquisition system, droplet generating unit and heater surface arrangement powered by a high capacity DC supply. The schematic of experimental set up is shown in Figure 1. A microfluidic pressure pump (Dolomite, Mitos P-pump) connected to an external air compressor, is used to generate the desired rate of droplets at the needle tip and are made to fall under gravity to achieve the required impact conditions. A trial set of 30 droplets is considered for diameter calculation and the generated droplet size is found to be 2.80 $\pm$ 0.04 mm.

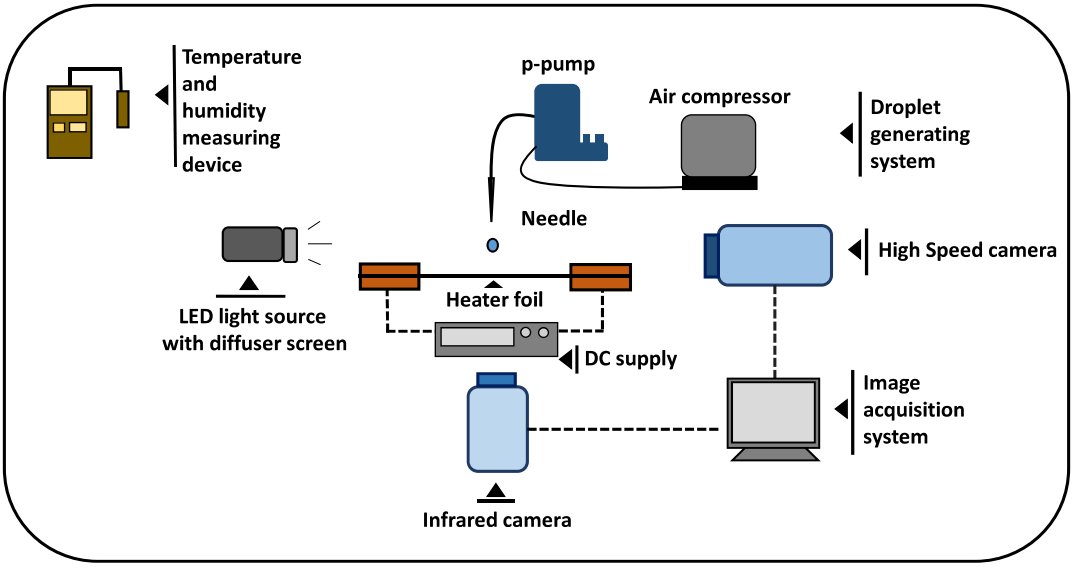

Figure 1: Schematic showing the experimental apparatus used in the present study

Image acquisition system consists of a high-speed camera (*Photron fastcam SA3 120K*) running at 10000 FPS (frames per second) with a spatial resolution of 20 μm/pixel. Shadow photography technique is adopted for imaging the droplets using a LED light source with a diffusion screen. Factory calibrated high-performance infrared camera (*FLIR X6540sc*) is used to capture the thermal foot print (temperature distribution) of the droplet on the surface. With a frame rate of 1000 FPS and a spatial resolution of 136 μ m/pixel, the infrared camera is triggered simultaneously along with high-speed camera. The post-processing of images is carried out using *Matlab* Image processing tool box and an open source java based image processing program, *ImageJ* [55].

An annealed Inconel 600 alloy foil of thickness 25 μm is used as the target surface, sandwiched between copper bus bars on either side, and fixed to a wooden base. The surface is polished, and the surface roughness measurement, R_a, using stylus probe profilometer is within the range of 0.15 - 0.30 μm. DC power supply (*BK Precision 1900, 1-16 VDC, 60 A*) is provided through the copper bus bars to maintain the surface at different temperatures using power supply controls. To improve the response of the infrared camera imaging of the surface, a thin layer of high heat-resistant black paint is applied underneath the surface. The emissivity of the paint was measured using an emissometer (*D & S Emissometer, Model AE*) and found to be 0.82. The dimensions of the foil surface is about 45 mm x 40 mm x 0.025 mm. Droplet impingement experiments were carried out at an ambient temperature of 22 °C and a relative humidity of about 50 %.

2.1. Impingement configuration

A train of two water droplets are consecutively impacted on to the foil surface. The event is captured through the high-speed camera from the side view while the temperature variation of the surface, upon interaction with the droplet, is acquired from the bottom of the surface using the thermal camera. The surface is hydrophilic, and contact angle measurements are made using *Holmarc's contact angle meter*. The static contact angle, quasi-static advancing and receding angles over the non-heated surface are 72 ± 1 °, 83 ± 4 ° and 13 ± 1 ° respectively. The impingement scenarios are presented in Figure 2 where both the schematic diagram and high speed images are provided.

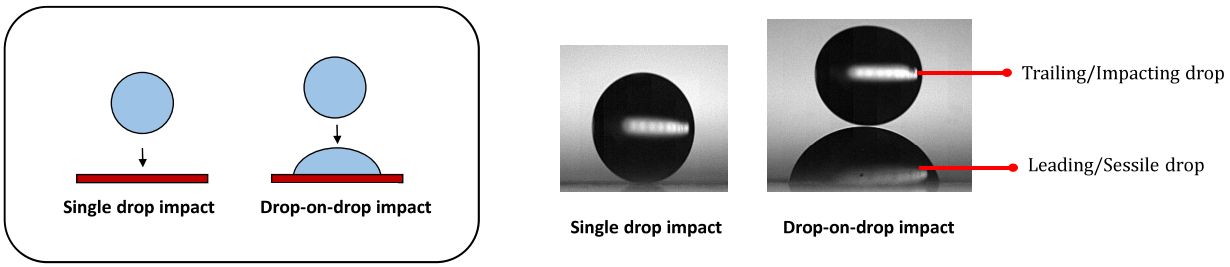

Figure 2: Impingement configurations considered in the present work

The time interval between the drops (δt_D) is approximately 3 seconds i.e., the flow rate is about 20 droplets per minute (dpm). With this flow rate, the leading droplet that impinges

the foil surface will become sessile, before the trailing droplet impacts on the sessile droplet. Thus the configuration can be treated as a drop-on-drop impact.

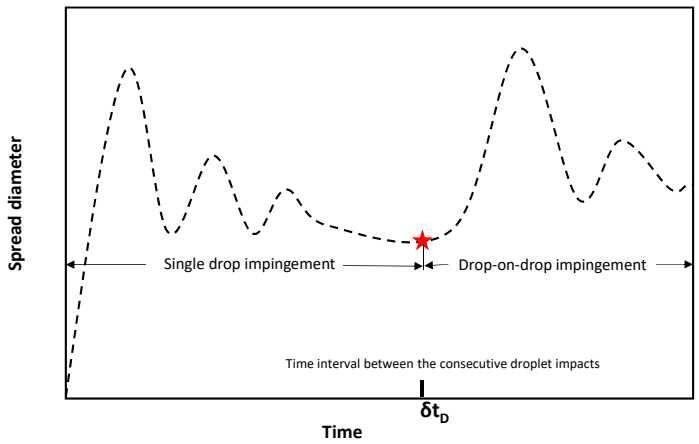

Figure 3: Schematic showing the temporal change of spread diameter during the impact

Figure 3 is a schematic that demonstrates the temporal change of droplet spread diameter upon impact with the surface. The first droplet, when impacted, oscillates on the surface for a while, and will remain sessile upon which the second droplet is impinged resulting in the spreading and receding phases, as shown in the Figure 3.

2.2. Image post-processing

Information regarding hydrodynamics such as droplet initial diameter (volume), spread diameter, and dynamic contact angle are measured using the side-view images of the impingement process. Standard procedures of image conversion i.e., conversion of grey to binary image followed by edge and region recognition, are implemented, and data is retrieved using resources available in *Matlab* and *ImageJ* post-processing toolbox. The resulting image after post-processing is shown in Figure 4.

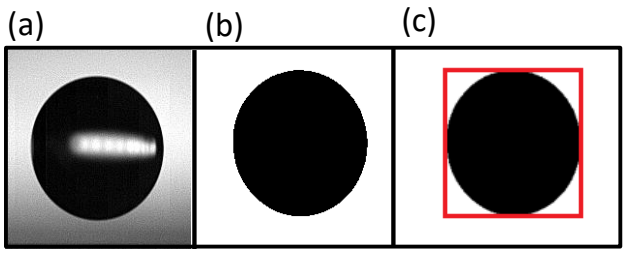

Figure 4: Steps involved in image post-processing: (a) Grayscale (b) Binary (c) Region recognition

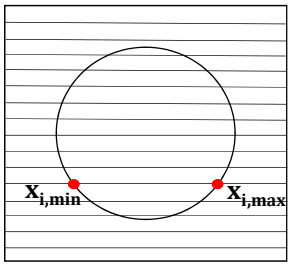

Figure 5: Droplet volume calculation

2.2.1. Droplet volume (diameter) calculation

High-speed images obtained from experiments are used for the calculation of droplet volume and diameter. Assuming an axi-symmetric droplet, the volume of the droplet is calculated [56] by summing up the cylindrical slices of unit pixel height as

$$Volume, V = \frac{\pi}{4} {Z_p}^3 \sum {d_i}^2 \tag{1}$$

where, d_i, the diameter of each cylindrical strip in the droplet image given as $(x_{i,max} - x_{i,min})$ as shown in Figure 5, and Z_p is the resolution of the image measured in $meter/pixels$

Then diameter of the droplet can be obtained as

$$Diameter, D = \left[\frac{6V}{\pi}\right]^{1/3} \tag{2}$$

2.2.2. Dynamic contact angle

The wetting characteristics of a surface for an impinging liquid can be represented using the contact angle in the three-phase contact region. Former studies on droplet-wall interactions [26, 57, 58] discussed various contact angles and the effect of contact line velocity and temperature on contact angle. Measurement of this dynamically changing angle will enhance the understanding of the key aspects associated with the spread and evaporation dynamics of the present work.

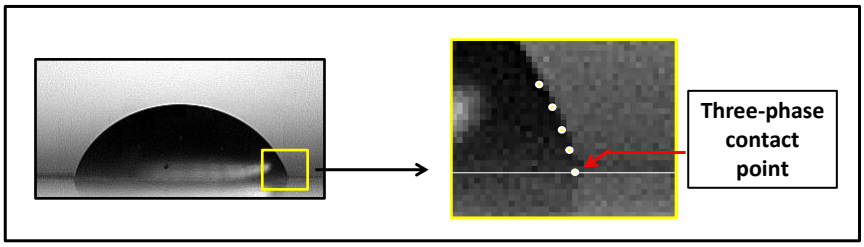

Figure 6: Contact angle measurement

In the present work, the three-phase contact angle is calculated using the side-view images of droplet impingement. During the impact process, the observed profiles of the droplet are complex, and standard methods of curve fitting for obtaining the droplet profile is mathematically tedious and complicated. Instead, as shown in Figure 6, at least five points on the droplet profile near the contact line region are considered. Upon analysis, a second-order polynomial fits well with the selected data points, and the tangent of the polynomial at the three-phase contact point is calculated as the dynamic contact angle.

2.3. Infrared image post-processing

The infrared camera used in the present study is factory calibrated, and the uncertainty associated with temperature measurement is $\pm$ 1 K. It is noticed that the recorded raw images are prone to noise, and is estimated in terms of the noise equivalent temperature difference (NETD) value of thermography system. For the given temperature range used in the study, the NETD values are within the acceptable range of 60 - 200 mK. However, it is shown that the heat conduction term used in the heat transfer analysis is sensitive to the spatial signal noise of the input temperature field [56] and extensive filtering is required to reduce the noise. Time and spatial averaging are applied to the temperature field, and it is followed by the application of *Matlab* provided Gaussian filter ($\sigma_{sd} = 2$). The detailed description of the method can be found in reference [56]. Figure 7(a) and (b) shows the raw and filtered heat flux image calculated during single droplet impact over a surface temperature of 154 °C, and at a time instant, t = 15 ms. From Figure 7(c), it is visible that the non-physical noise in heat flux distribution is reduced, and the overall droplet heat transfer during the impact, expressed as effectiveness (Q^*), is not significantly affected by the filtering procedure, as given in Figure 7(d).

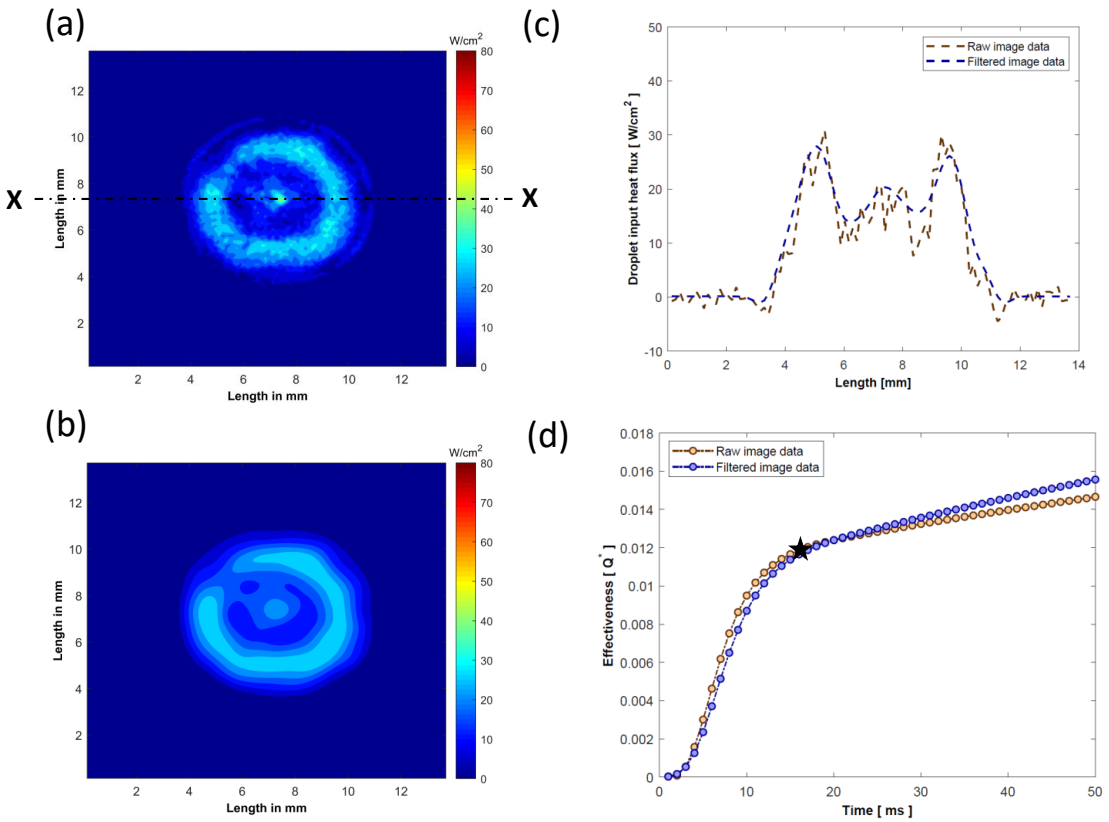

Figure 7: (a) Raw image (T = 154 °C and t = 15 ms) (b) Filtered image (c) Droplet input heat flux distribution along the centreline X-X (d) Effectiveness

2.3.1. Droplet input heat transfer calculation

The droplet input heat transfer is one of the important parameters required for understanding the droplet-hot wall interactions and the ongoing cooling process. The temperature variation of the surface is obtained from the bottom of the surface via infrared images. An energy balance is applied at every pixel element of the surface, as shown in Figure 8 to calculate the heat transfer into the droplet.

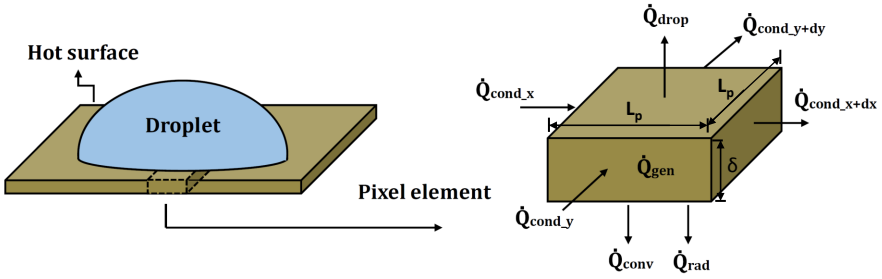

Figure 8: Heat transfer calculation: energy balance at a pixel element

The energy balance applied to the pixel element results in

$$Q_{stored} = Q_{gen} + Q_{cond} - Q_{rad} - Q_{conv} - Q_{drop} \tag{3}$$

where droplet input heat transfer is represented as Q_{drop}

Thus,

$$Q_{drop} = Q_{gen} + Q_{cond} - Q_{rad} - Q_{conv} - Q_{stored} \tag{4}$$

and droplet input heat flux q_{drop} is obtained, using the length of the pixel element L_p, as

$$q_{drop} = \frac{Q_{drop}}{L_p^2} \tag{5}$$

It is noted that Q_{stored} represents the change in energy of the surface due to cooling, and Q_{gen} being heat generated due to DC supply. While Q_{cond}, Q_{rad} and Q_{conv} are net conduction heat transfer along the surface, radiation and convection heat transfers underneath the surface respectively. Further details for obtaining each term in the energy balance is provided in the appendix.

Using the above energy balance, the contributions of heat transfer quantities towards the droplet input heat transfer is compared. Two instants, one each in the spreading and receding phase, are selected and the percentage of heat transfer quantities is calculated against the magnitude of droplet input heat transfer at the impact point (pixel). Figure 9 shows the selected points which are marked over the temporal change of spread factor for the droplet impingement over the surface at a temperature of 154 °C. Figures 10 and 11 present the comparison of these quantities during the advancing and receding phases as a percentage

of the droplet heat transfer. It is evident that Q_{gen} and Q_{cond} are significant quantities compared to Q_{rad} and Q_{conv} in contributing to the droplet input heat transfer.

Even though the heat loss by convection and radiation seems negligible in receding phase, it is important for the accurate estimation of droplet heat transfer in the spreading phase. Thus, in the present work, all the above described heat transfer quantities will be included for droplet heat transfer calculations.

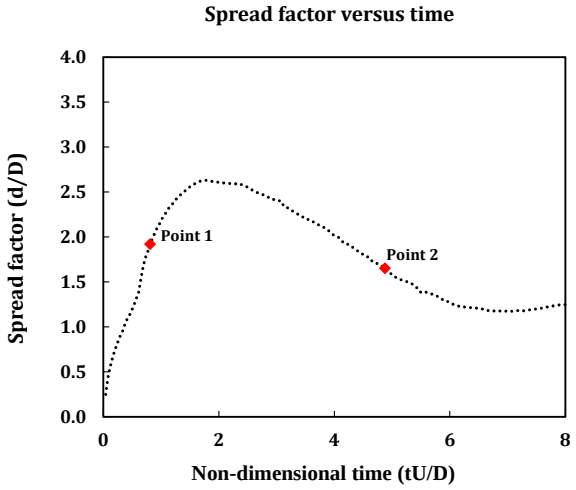

Figure 9: Single droplet impact over the target surface (T = 154°C)

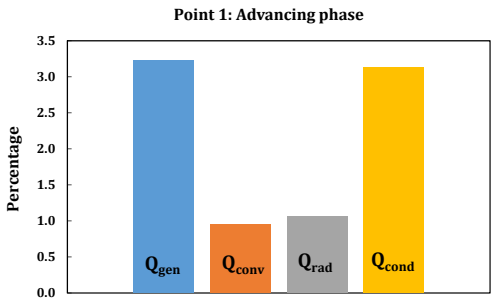

Figure 10: Comparison in advancing phase

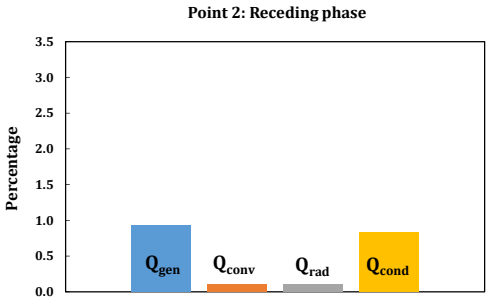

Figure 11: Comparison in receding phase

2.4. Experimental methodology: Validation cases

The present experimental methodology is validated using previously published studies available in the literature. Two cases: drop-on-drop impingement over a non-heated surface, and a single droplet impact over a heated surface are carried out. The spreading parameter i.e., spread factor is calculated and compared with experimental results.

2.4.1. Drop-on-drop impact over non-heated surface

For the present study, the generation of multiple droplets to achieve the drop-on-drop configuration is crucial. Wakefield et al. [59] carried out drop-on-drop impingement studies over a non-heated Teflon surface with the Weber number as a parameter. A case with Weber number of 2 is considered for the validation, and the results are compared in terms of the spread factor. Figure 12 shows the results from the present experiments compared with Wakefield et al. [59]. The variation of spread factor with time was found to be in agreement within $\pm$ 10 %, thus validating the experimental methodology followed in the present work.

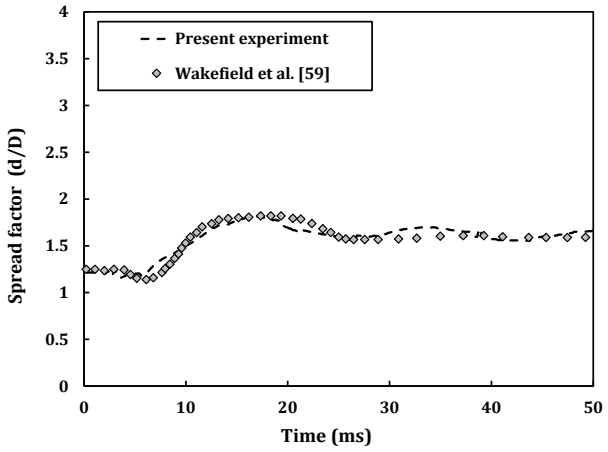

Figure 12: Drop-on-drop impact over a non-heated surface

2.4.2. Single droplet impact over a heated surface

Pasandideh-Fard et al.[23] studied the cooling effectiveness of a single droplet over a heated surface. A single water droplet is impacted over a stainless steel surface maintained at a constant temperature of 120 °C with an impact Weber number of 47. In the present set up, a thin Inconel surface is used instead of stainless steel, and maintained at 120 °C. Figure 13 shows the temporal variation of spread factor during the impingement. To validate the accurate variation of spread dynamics over a heated wall, the surface temperature and impact conditions should be exactly maintained. However, inspite of the differences in the target surface (Inconel versus Stainless steel), the results shown in Figure 13 show similar trends confirming the validity of the present experimental set-up for droplet impingement studies over heated target surfaces.

Table 1: Thermo-physical properties of the deionized water used in the present study, at 1 atm and ambient temperature of 22 ° C.

Properties	Value
Saturation temperature ,T_{sat}, ° C	100
Density, ρ_l, kg/m^3	998
Dynamic viscosity, μ, Ns/m^2	0.001
Surface tension, σ, N/m	0.0725
Specific heat capacity, c_p, kJ/kgK	4.18
Latent heat of vaporization, h_{lv}, kJ/kg	2260

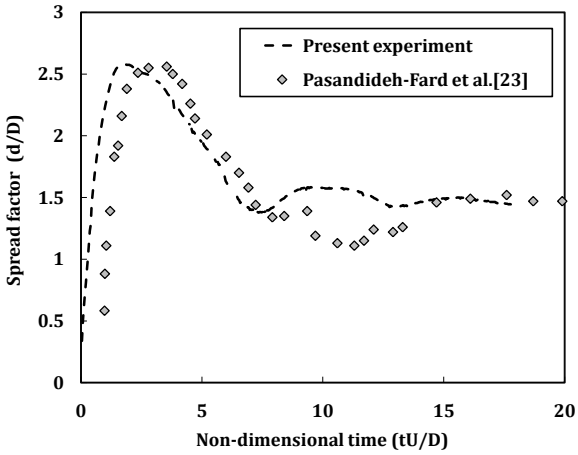

Figure 13: Single droplet impact over a heated surface (T = 120 °C)

3. Present experimental investigation

During the present investigation, a train of two water droplets of diameter 2.8 mm is impacted, with a velocity of 1.138 m/s, onto a thin Inconel surface maintained at a constant temperature. The thermo-physical properties of the deionized water and Inconel surface are listed in Table 1 and Table 2 respectively. The impact conditions corresponds to a Weber number of 50 and Reynolds number of 3180 with a constant flow rate of 20 droplets per minute (DPM). The surface temperature is the parameter and varies from 22 °C (non-heated) to 175 °C. At every temperature, the images of single drop and drop-on-drop impacts are recorded separately and analysis is carried out. Here the focus is to analyze the spread and heat transfer characteristics at the instant of impact where effective cooling of the surface will take

Table 2: Thermo-physical properties of the Inconel 600 alloy used in the present study.

Properties	Value
Density, ρ, kg/m^3	8470
Thermal conductivity, k_s, W/mK	14.8
Electrical resistivity, ρ_s, Ohm-m	$103 \cdot 10^{-8}$
Specific heat capacity, c, kJ/kgK	444
Temperature coefficient of resistance, α_s , K^{-1}	$12 \cdot 10^{-5}$

Table 3: The experimental uncertainties associated with different parameters used in the study. Here ΔX represents the absolute uncertainty where as Δx stands for the relative uncertainty.

Parameter	Uncertainty
Temperature	ΔX = $\pm$ 1 K
Generated volumetric heat flux [56]	Δx_{max} = 11 %
$q''_{gen} = Q_{gen}/V_s$	($q''_{gen} = 20 \cdot 10^6$ W/m^3 at T = 50 $^\circ$ C)
Weber number, We	ΔX = $\pm$ 2 ($We = 50$)
Reynolds number, Re	ΔX = $\pm$ 90 ($Re = 3180$)
Droplet diameter, D	ΔX = $\pm$ 0.04 mm ($D = 2.8mm$)
Droplet impact velocity, U	ΔX = $\pm$ 0.0171 m/s ($U = 1.138m/s$)
Dynamic contact angle, θ	Δx_{max} = 36 % ($\theta = 62^\circ$ at T = 175 $^\circ$ C, Single droplet impact)
	Δx_{min} = 1.2 % ($\theta = 81^\circ$ at T = 175 $^\circ$ C, Drop-on-drop impact)
Spread factor , S^*	Δx_{max} = 12 % ($S^* = 0.43^\circ$ at T = 175 $^\circ$ C, Single droplet impact)
	Δx_{min} = 2 % ($S^* = 2.63$ at T = 175 $^\circ$ C, Single droplet impact)

place. The time scale of impingement is of order; time t = 45 milliseconds corresponds to a non-dimensional time, $\tau = 18$ for each configuration. The spread dynamics is photographed using a high-speed camera, and the temperature response during the impact is recorded from the underside of the surface using infrared thermography.

At each chosen temperature, three sets of data is recorded (n = 3), and average values are used to represent the data. The experimental uncertainties associated with different parameters are presented in the Table 3. Here ΔX and Δx are used to represent the absolute and relative uncertainties respectively.

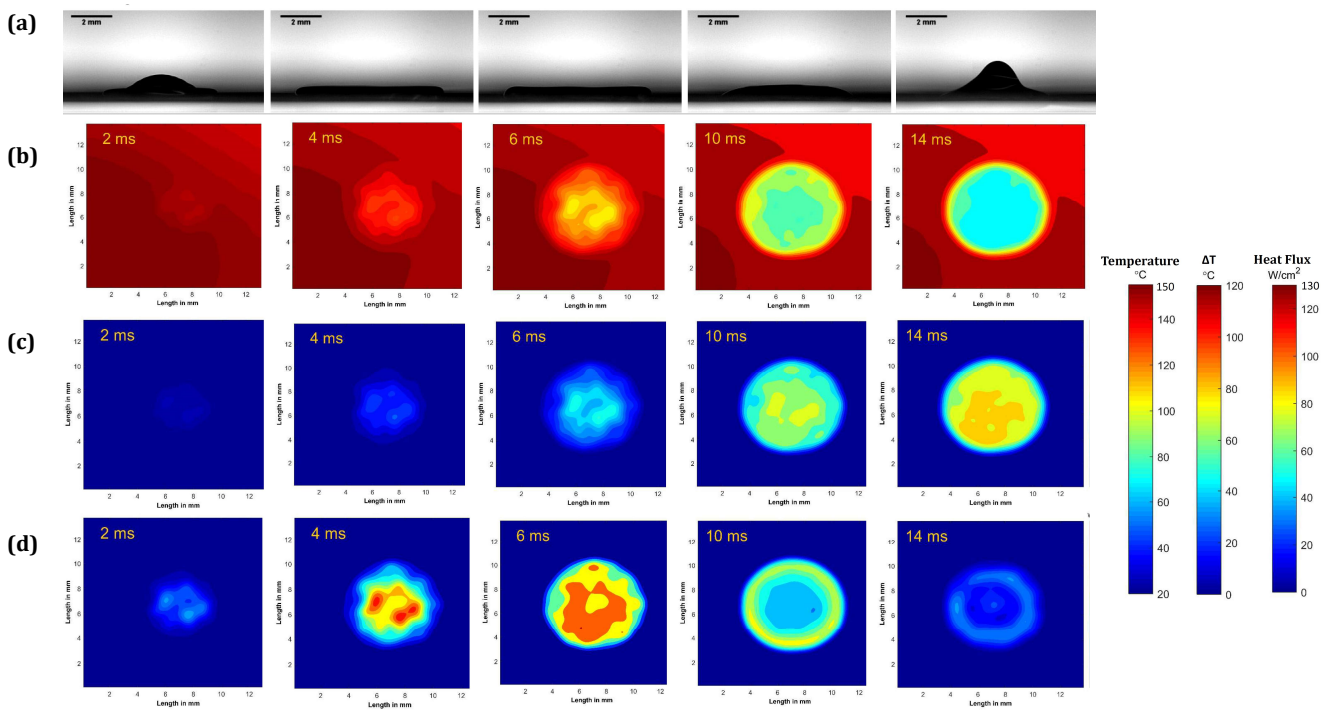

Figure 14: Single droplet impingement over the foil surface (T = 154 °C) : (a) Side-view image (b) Foil surface temperature after impingement (c) Change in temperature (d) Heat flux distribution

4. Results and Discussion

When the droplet comes in contact with a hot surface, heat transfer takes place which results in the cooling of the surface. The temperature of the droplet increases with time; evaporation ensuing across the liquid-gas interface affects the droplet spread diameter. Thus, it is important to study the effect of surface temperature on both the spread and the heat transfer characteristics. Figures 14 and 15 show the spread behaviour of single and drop-on-drop configurations, respectively over the surface with a pre-impact surface temperature of 154 °C. The present arrangement of hot surface, using Joule heating, resulted in slightly non-uniform pre-impact surface temperature. Here, the spatial mean temperature (maximum deviation of ± 3 °C is observed at T = 154 °C) is represented as the surface temperature. Also, to realise the temperature contours during drop-on-drop impact, the change in temperature (ΔT) for each pixel, is calculated as the difference of the initial temperature to the instantaneous temperature. The temperature contours, the corresponding change in temperature (ΔT), and droplet input heat flux (q_{drop}) are also presented. A considerable amount

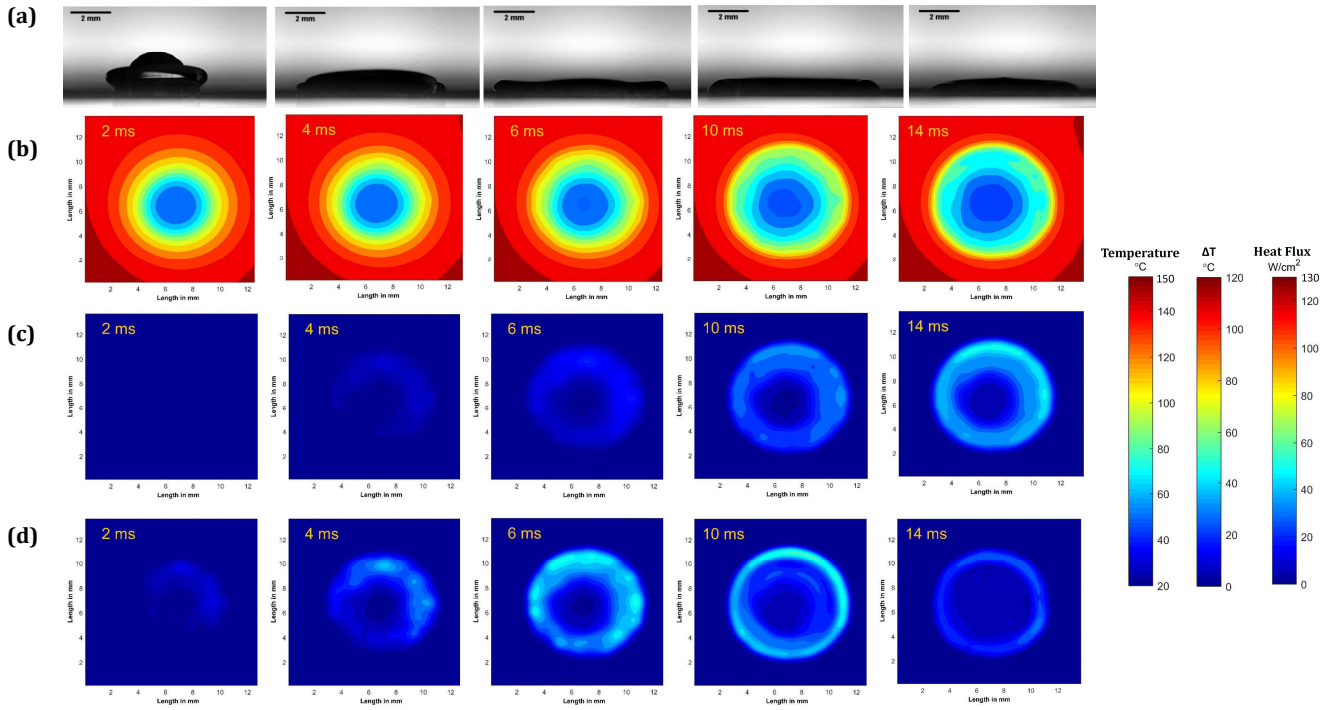

Figure 15: Drop-on-drop impingement over the foil surface (T = 154 °C) : (a) Side-view image (b) Foil surface temperature after impingement (c) Change in temperature (d) Heat flux distribution

of heat transfer, termed as effective heat transfer, is observed to occur during the initial stage of droplet interaction with the surface in both the configurations. From Figures 14 (d) and 15 (d), it can be noted that the significant heat transfer is during the initial spreading phase whereas the peak value is detected at the maximum spread of the droplet. However the heat transfer associated with single droplet impact is prominent compared to that of drop-on-drop configuration. This is because of the low pre-impacting surface temperatures for drop-on-drop scenario as given in 15 (b), due to the presence of the initial droplet on the target surface, thereby resulting in lower heat transfer rates. The subsequent sections of this paper describe the spread hydrodynamics in terms of the spread factor and surface wetting i.e., contact angle. Detailed description of heat transfer characteristics are also provided.

4.1. Spread hydrodynamics

Upon impact, the leading droplet performs a series of advancing and receding phases by dissipating the impact energy and attains a sessile droplet state. Consecutively, the second droplet, which impinges on to the sessile droplet, will coalesce for specific instant followed

by the spreading and receding phases. Thus, for a single droplet impact, the initial cycle consists of two phases; advancing and receding. Whereas, in a drop-on-drop impingement, three stages, namely; coalescing, advancing and receding, are identified during the initial cycle. A non-dimensional quantity called spread factor, S^*, is defined as the ratio of spread diameter at an instant (d) to the pre-impact droplet diameter (D). The temporal variation of spread factor during single droplet and drop-on-drop impact, with identified phases at various surface temperatures, is plotted, as shown in Figure 16. For both the configurations, the temperature effect on the spread is evident from the first cycle of spreading. Also, there is a notable reduction in spread factor with temperature in subsequent cycles for both the single droplet as well as drop-on-drop impingement configuration. The comparison of spread

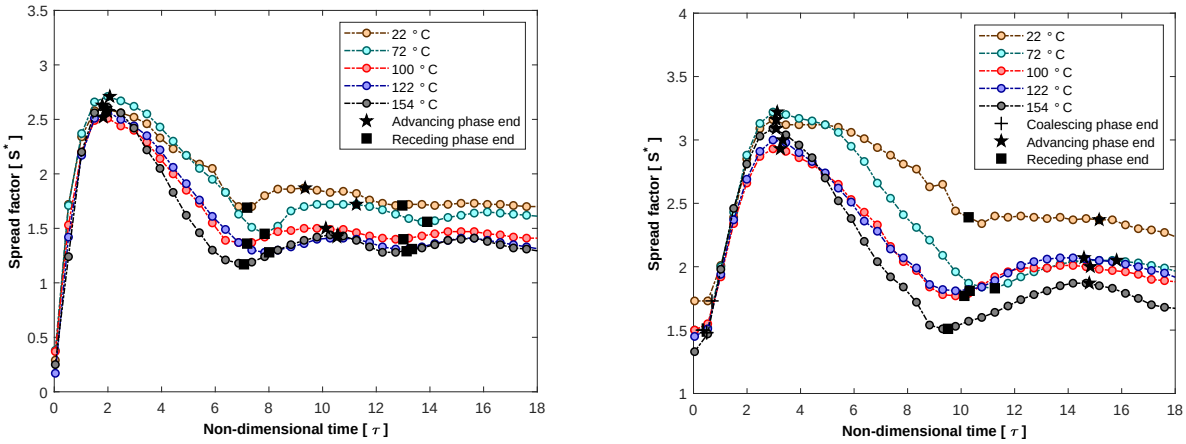

(a) Single drop impingement

(b) Drop-on-drop impingement

Figure 16: Spread factor versus time

factor during single droplet and drop-on-drop impact at a surface temperature of 154 °C is obtained to understand the effect of configuration on hydrodynamics, as shown in Figure 17. Due to the interference of droplets during the impact, the cycle of spreading and receding is delayed, for drop-on-drop impingement, which resulted in longer initial cycle time. The cycle time of single droplet impact is about t = 18 ms ($\tau \sim 7.5$) and drop-on-drop impingement is about t = 24 ms ($\tau \sim 9.5$) where coalescing phase is about t = 1 ms ($\tau \sim 0.5$). The presence of two droplets resulted in a higher spread factor for the drop-on-drop configuration. However, the *net spread factor* (δS^*) at a given instant of time, which is defined as the ratio of change in spread diameter ($d - D_s$) to the impacting droplet diameter (D), is more for the single

droplet case. The *net spread factor* has reduced during the drop-on-drop impingement due to the high energy dissipation resulted from the droplet coalescence.

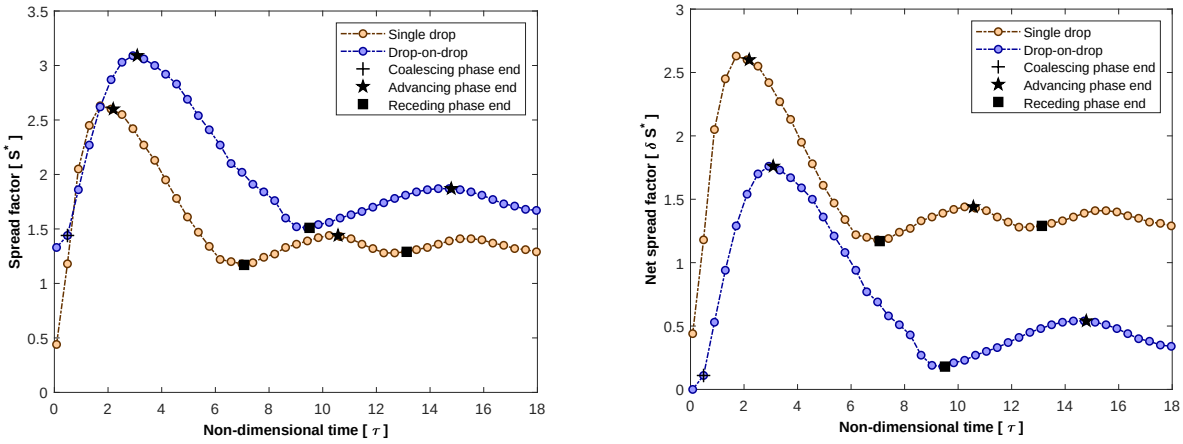

(a) Spread factor versus time

(b) Change in spread factor versus time

Figure 17: Comparison of single and drop-on-drop impact over the surface (T = 154 °C)

Observations revealed that the dynamics of spread is coupled with droplet heat transfer. Especially, the maximum spread factor will dictate the extent of heat transfer over the surface. So, in order to analyse heat transfer rate, the maximum spread factor for the initial and second cycle of the post-impingement is considered. It is noted that, in the present context, a cycle refers to a sequence of spreading and receding phases. Figures 18 (a) and 18 (b) shows the comparison of maximum spread factor during the first and second cycles which convey that the initial cycle's maximum spread factor has a weak dependence on the surface temperature, whereas it decreases with temperature during the second cycle and the effect is significant for both configurations during the second cycle.

Likewise, another important parameter related to hydrodynamics is the contact angle and its variation during both impingement configurations. The three-phase contact angle is known to vary with velocity [57] and increase with the surface temperature [26, 58]. It will affect the spread of the droplet, and therefore, the heat transfer rate. The variation of the dynamic contact angle with time is obtained for the present configurations to ascertain the effect of temperature, as shown in Figure 19. As soon as the droplet impacts the surface, a high contact angle is observed as it is under the influence of impacting velocity, and the value declines during the receding phase [57]. In the present study, the captured contact angle

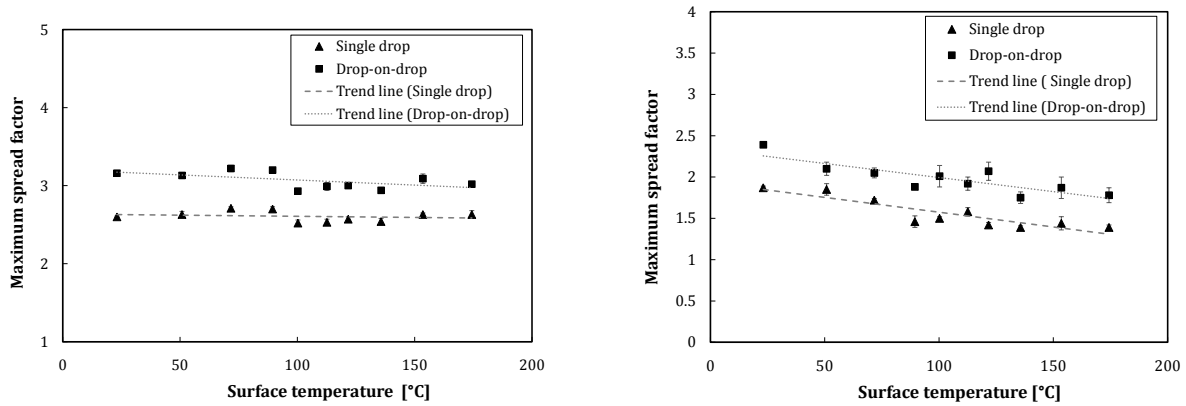

(a) Cycle 1

(b) Cycle 2

Figure 18: Maximum spread factor with surface temperature: Single drop and drop-on-drop impact

variation exhibits a similar behaviour during both impingement configurations, as shown in Figures 19(a) and (b).

For a single droplet impact, the contact angle is increased till it reaches the maximum spread (advancing phase end) and decreases to a minimum angle at the end of receding phase which is given in Figure 19(a). Meanwhile, for drop-on-drop impingement, as presented in 19(b), the trend is similar to single droplet impact, additionally exhibits a constant angle during the coalescing stage. In the present study, the effect of temperature on dynamic contact angle is found to be weak. During the single droplet impingement, a slight increase in dynamic contact angle is observed for the heated case (T = 175 °C) compared to non-heated case (T = 22 °C) in subsequent stages of spreading as shown in Figure 19(a). However, the increase is marginal and within the uncertainty of the presented data. Additionally, sessile droplet contact angle (Static contact angle) variation with surface temperature is inspected and given in Figure 20, and for the temperatures used in the present work, there is only a minor increase in contact angle with surface temperature. Previous studies [26, 58] reported a strong effect of temperature on contact angle which is not so evident in the present work. The difference in volatility of the liquid, and surface conditions are attributed to this behaviour.

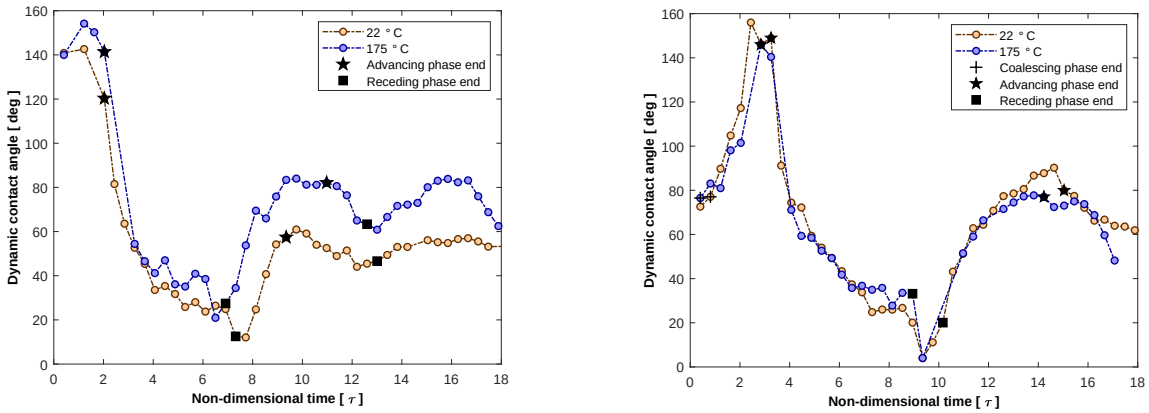

(a) Single drop impingement

(b) Drop-on-drop impingement

Figure 19: Dynamic contact angle versus time

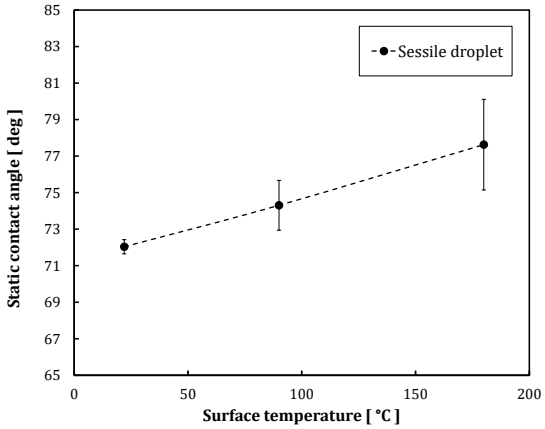

Figure 20: Static contact angle versus temperature

4.2. Heat transfer characteristics

Furthermore, to understand the heat transfer into the droplet, an average quantity of heat transfer is calculated over an effective area in which a significant amount of heat transfer takes place. The effective area is identified using Canny edge detection technique, implemented in *Matlab* image post-processing toolbox, applied to a heat flux image [60] as shown in Figure 21. A dimensionless effective area $A_e{}^*$ is used to compare the present impingement configurations. This is calculated as the ratio of the surface area with effective heat transfer to the cross-sectional area of the impacting droplet.

$$A_e^* = \frac{4A_e}{\pi D^2} \tag{6}$$

where A_e is the area where effective heat transfer is observed. In the present work, dimensionless effective area ${A_e}^*$ provides a quantitative measurement of area being cooled during the impingement and it can also be observed that the maximum spread factor ${S^*}_{max}$ during the impact can be approximated from the effective area as

$${S^*}_{max} \sim \left(({A_e}^*)_{max}\right)^{0.5} \tag{7}$$

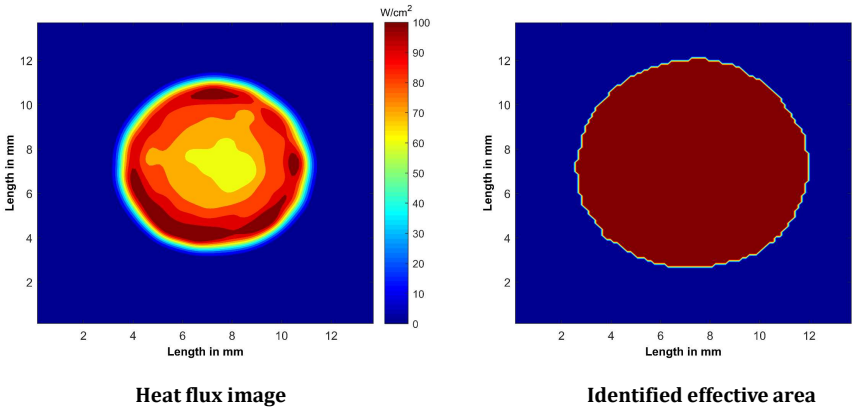

Figure 21: Effective area recognition to calculate the average surface heat transfer rate

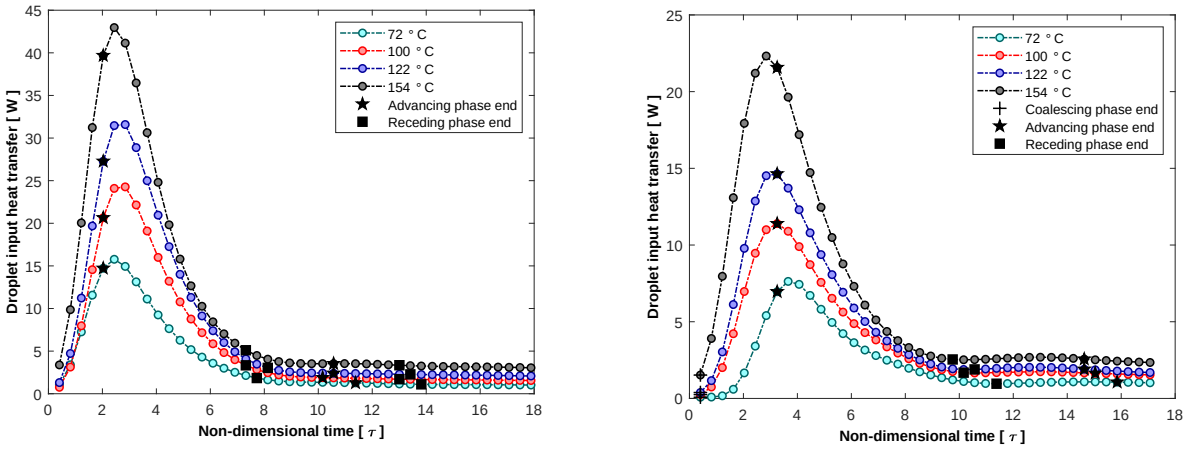

(a) Single drop impingement

(b) Drop-on-drop impingement

Figure 22: Droplet input heat transfer versus time

Figure 22 shows that the droplet heat transfer is enhanced with an increase in the surface temperature and this trend is similar for both single and drop-on-drop configurations. A maximum in droplet heat transfer rate is realised at the end of the first advancing phase for all surface temperatures and confirms that most of the surface cooling is takes place during the initial cycle of the droplet impact. A dimensionless input heat transfer, termed as effectiveness or cooling efficiency (Q^*), is introduced to estimate the overall heat transfer per droplet. It is defined as the ratio of the time integral of droplet input heat transfer to the total heat required for the droplet evaporation.

$$Q^* = \frac{\int_0^t (Q_{drop})dt}{m(c_p(T_{sat} - T_\infty) + h_{lv})} \tag{8}$$

Figure 23 shows the variation of effectiveness (Q^*) with time for both single and drop-on-drop impingement at different temperatures.

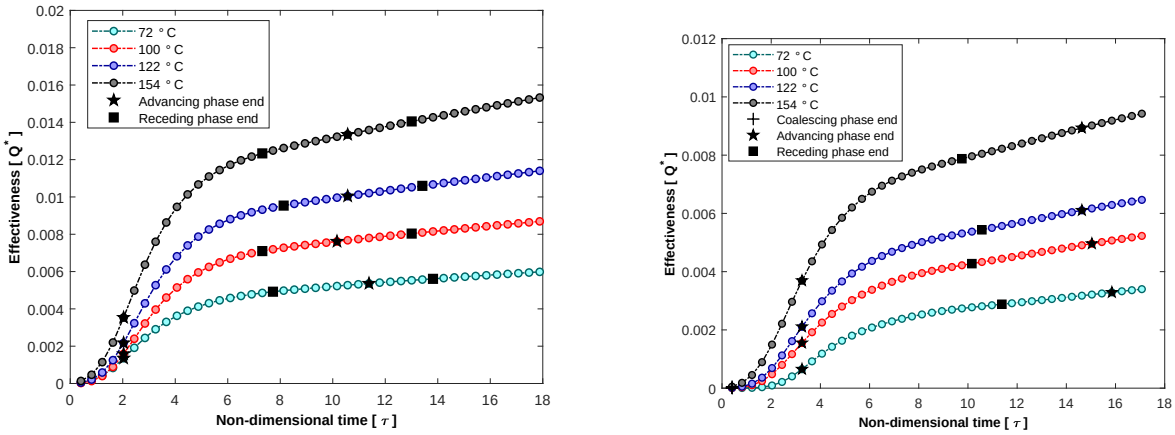

(a) Single drop impingement

(b) Drop-on-drop impingement

Figure 23: Effectiveness versus time

A comparison of both the configurations at a given surface temperature, as shown in Figure 24, reveals that the droplet input heat transfer is lower for the drop-on-drop impact compared to single droplet case. This is because of the reduction in surface mean temperature as a result of initial droplet (sessile) interaction with the surface. Also, the previous work using numerical modelling [53] revealed that there is rapid decline in heat transfer rate due to the increased film thickness during the drop-on-drop impingement.

In order to interpret the surface cooling during the impingement, the surface temperature change with time is determined. The surface temperature change upon impact is plotted by

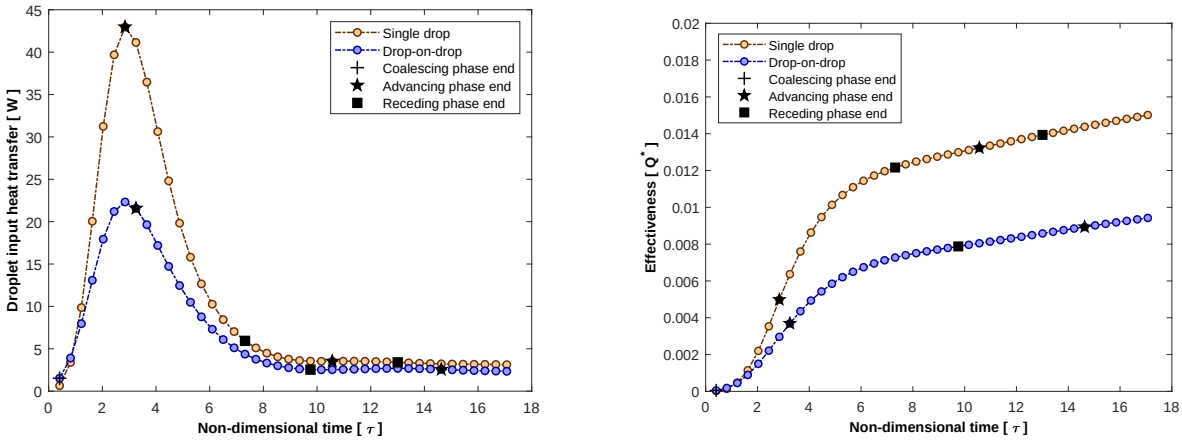

(a) Droplet input heat transfer versus time

(b) Effectiveness versus time

Figure 24: Comparison of single and drop-on-drop impact over the target surface (T = 154 °C)

tracking the temperature of the impact point, and termed as centre temperature as shown in Figure 25. The impact point is always the lowest temperature over the surface during the impingement [23]. The change in surface temperature is rapid for the case of single droplet impingement compared to drop-on-drop impact, and follows a similar trend for all surface temperature cases considered in the study. However, it is observed that the effective area where considerable heat transfer occur, is improved during the drop-on-drop impingement as shown in Figure 26.

In addition, a mean surface temperature is required to represent the overall surface cooling, and is calculated considering the effective area. Figure 27 represents the mean surface temperature variation with time at different temperatures. As given in Figure 28, the comparison reveals that the overall cooling is significant for the first (single) droplet impact compared to the drop-on-drop impact configuration. Nevertheless, as shown in Figure 26, it should be noted that the area being cooled, is improved during the drop-on-drop impact.

The present study investigates two configurations of droplet impingement: single droplet as well as the drop-on-drop. The pre-impacting surface temperatures are different for drop-on-drop impact, compared to that of single droplet impact. Therefore, a dimensionless temperature, T^* is defined and given as,

$$T^* = \frac{T_i - T_f}{T_i - T_\infty} \tag{9}$$

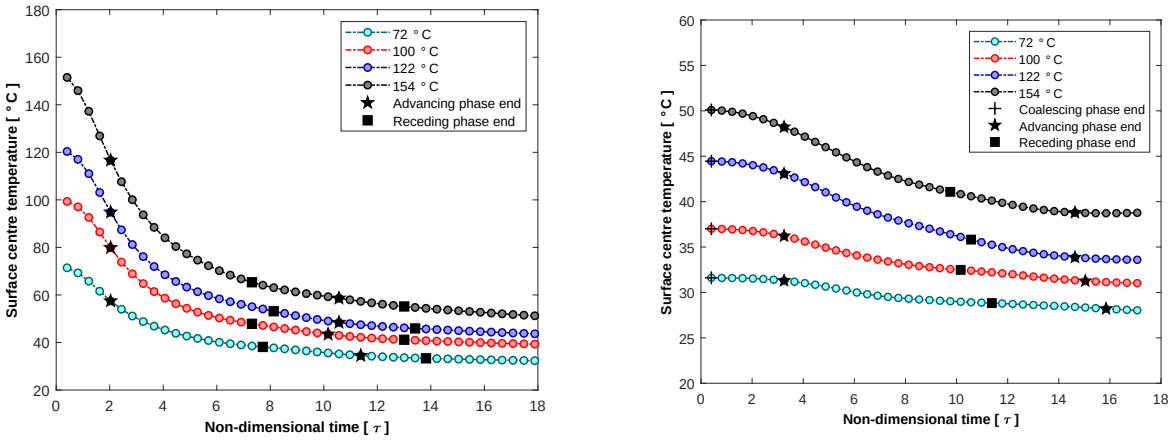

(a) Single drop impingement

(b) Drop-on-drop impingement

Figure 25: Target surface center temperature versus time

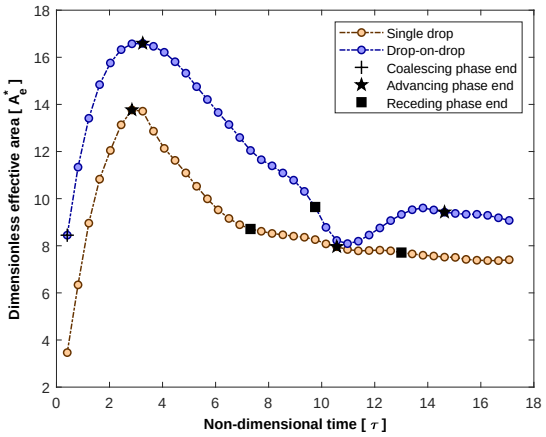

Figure 26: Comparison of effective area for the target surface (T = 154 °C)

where T_i ,T_f are initial and final surface temperatures respectively and T_∞ being the ambient temperature, in order to compare the two configurations considered in the present study.

Figure 29 (a) and (b) shows the distribution of dimensionless temperature at the instant of maximum spread during the single droplet and drop-on-drop impact over the surface with a temperature of 154 °C respectively. The comparison of the dimensionless temperature along the identified centreline is given in Figure 29 (c). For the single droplet, dimesnionless temperature (T^*) of about 0.3 is observed in the interacted area. Whereas, in the case of drop-on-drop impact configuration due to the presence of sessile droplet, the cooling

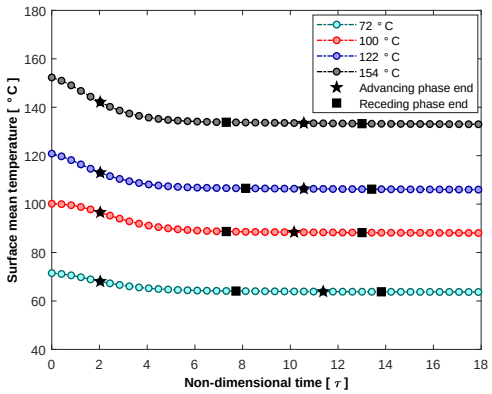

(a) Single drop impingement

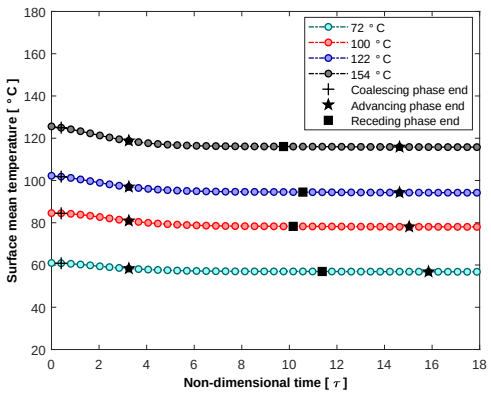

(b) Drop-on-drop impingement

Figure 27: Surface mean temperature versus time

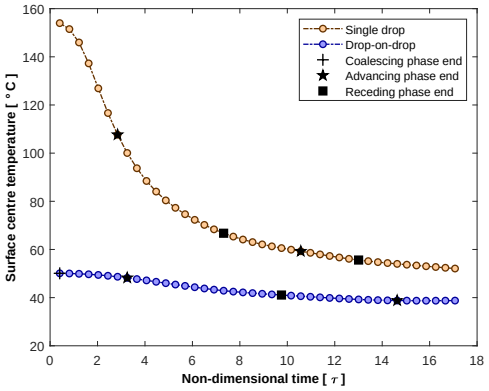

(a) Surface centre temperature versus time

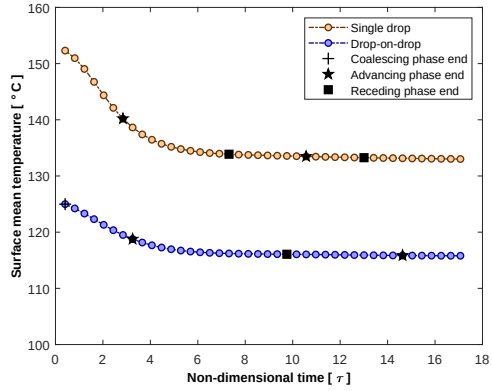

(b) Surface mean temperature versus time

Figure 28: Comparison of single and drop-on-drop impact over the surface with temperature 154 °C

effect has reduced, with a T* Value of 0.1 in most of the spreading region. However the surface cooling has improved ($T^* \sim 0.3$) in the peripheral of the droplet spread. Thus, the investigation confirms that there is always a decline in cooling effect by the trailing droplet during drop-on-drop impingement.

To quantify the heat transfer characteristics of the impingement configurations considered in the study, an effectiveness ratio (ϵ) is used which is defined as the ratio of dimensionless heat input during the drop-on-drop impact to that of a single droplet impact.

$$\epsilon = \frac{(Q^*)_{drop-on-drop}}{(Q^*)_{single}} \tag{10}$$

It provides a better understanding of each droplet performance (during consecutive droplet impact) in cooling the surface at different wall superheats, and the effect of droplet coales-

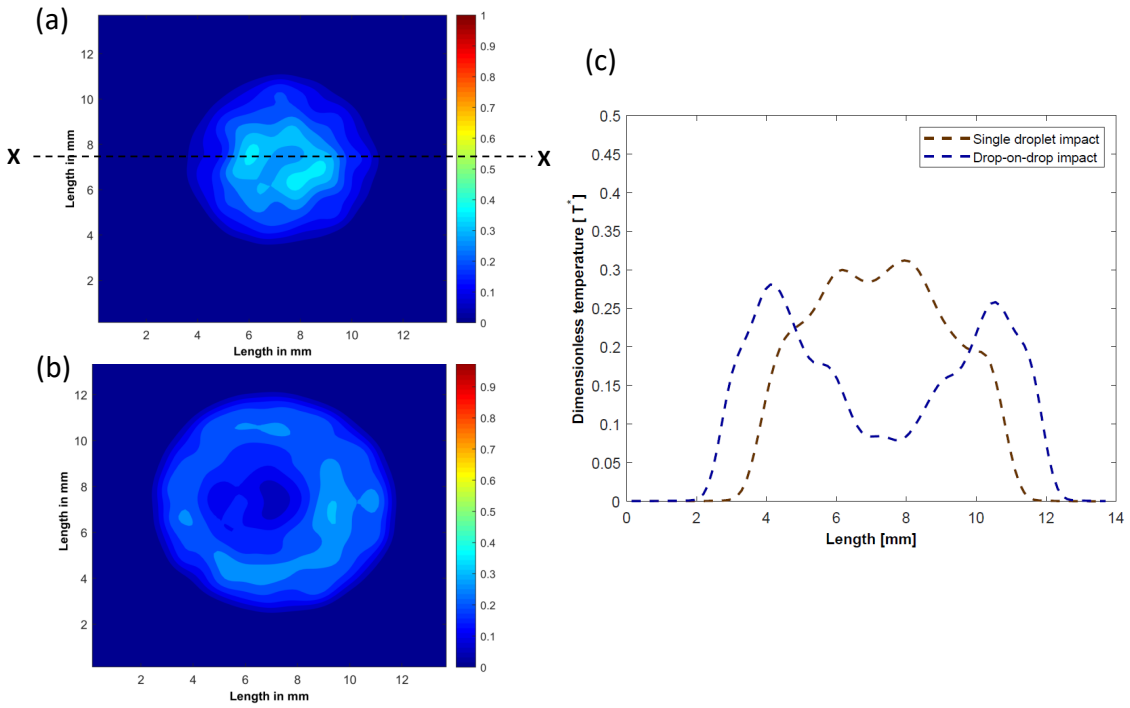

Figure 29: Comparison of dimensionless temperature (at T = 154 °C) (a) Single droplet impact (b) Drop-on-drop impact (c) Distribution along the centreline X-X

cence on spread and heat transfer characteristics during the impingement. Figure 30 shows the effectiveness ratio for different surface temperatures. The ratio is found to be nearly constant around a value of 0.62 for all observed temperatures. It can be inferred that the heat transfer for a trailing droplet is always lower compared to a leading droplet during the drop-on-drop configuration. The pre-cooling of the surface caused by the initial droplet, reduces the surface mean temperature, and thereby decreases the heat removal rate of the trailing droplet. It is worth noted that the magnitude of reduction in heat transfer could be influenced by the droplet flow rate, which controls the surface mean temperature. Also, the boiling regimes such as nucleate boiling with rigorous bubbles, and film boiling, can determine the outcomes of drop-on-drop impingement phenomenon. In the present work, the flow rate was constant at 20 droplets per minute (DPM), and the adopted surface temperatures are not adequate to initiate the bubbles (of nucleate boiling) in the droplet. Further investigations are needed to analyze these parameter effects on the spread and evaporation dynamics.

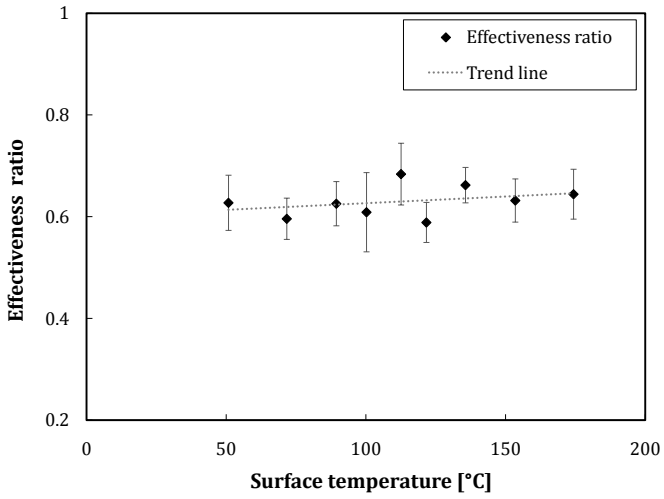

Figure 30: Effectiveness versus temperature

4.3. Three-phase contact line region: Temperature and heat flux distribution

Figure 31 shows the temperature and heat flux distribution of the target surface during single droplet and drop-on-drop impact at an instant. The spread diameter estimated from the high speed image is superimposed onto the infrared temperature and heat flux images. It is observed that the surface temperature increases in the radial direction from the center of the droplet (impact point). For both configurations, the maximum heat flux value is recorded in the vicinity of three-phase contact line as shown in Figure 31 and is found to be significant in receding phase. Low film thickness near the contact line region is attributed to the observed high heat transfer rates. For the case of drop-on-drop impingement, Figure 31(b) also unveils that there is an effective heat transfer in the annulus portion i.e., the region of change in spread and thereby extends the area being cooled. These observations will be used in further sections to develop a model for estimating droplet heat transfer during impingement.

4.4. Analytical modelling

4.4.1. Maximum spread

Earlier studies [23, 58, 59] modelled the maximum spread theoretically using the energy conservation principle. Two instances during the droplet impingement are considered i.e., pre-impact state and the instant of maximum spread. The associated kinetic, potential

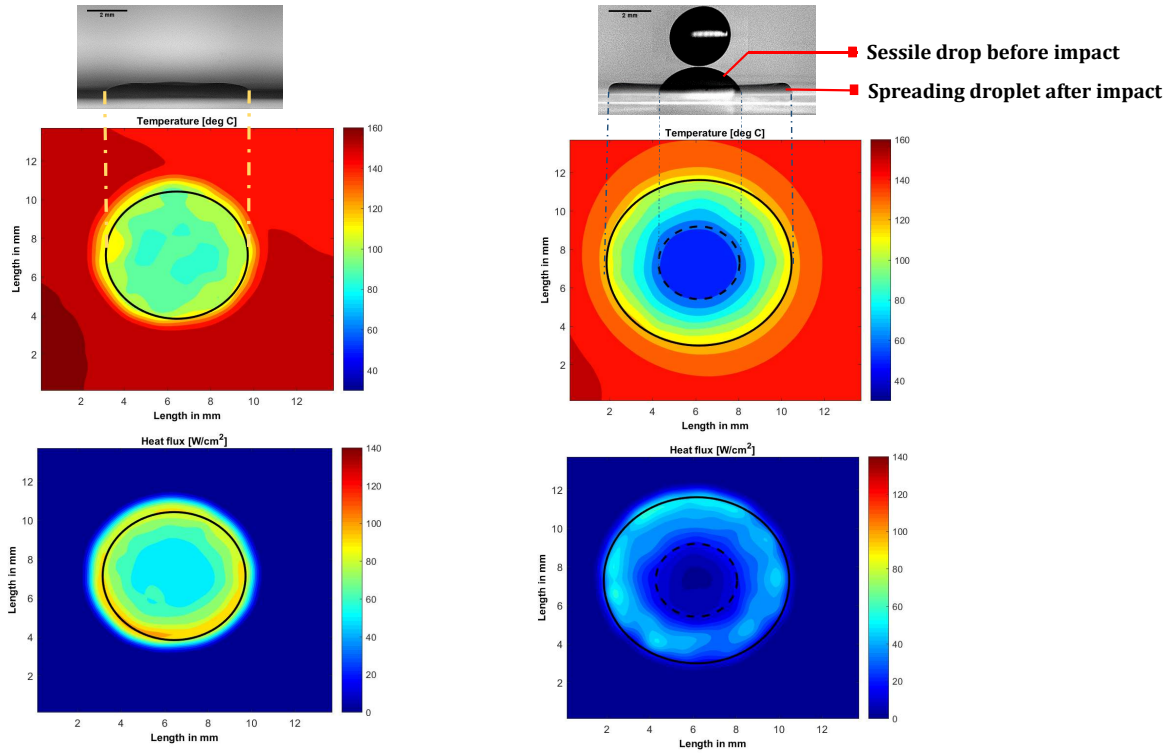

(a) Single drop impingement

(b) Drop-on-drop impingement

Figure 31: Post-impact behaviour over the target surface (T = 154 °C; t = 8 ms)

and surface energies are taken into consideration to estimate the maximum spread factor. The theoretical models proposed in the literature are adopted in the present work in order to validate the present experimental observations. Batzdorf [61] implemented an analytical model for evaluating the maximum spread during the single droplet impact over a hot surface. A schematic of the droplet system with the initial and final states considered are presented in Figure 32. Using energy balance it is shown [61] that the maximum spread can be calculated from following equation.

$$We + 4Bo + 12 - 3(1 - cos(\theta_{max}))S^{*2}_{max} = \frac{9a}{2}\frac{We}{Re(1 - Q^*_e)}S^{*4}_{max} \tag{11}$$

where θ_{max} and Q^*_e are contact angle at the instant of maximum spread and dimensionless evaporated mass, respectively. The dimensionless evaporated mass (Q^*_e) is given as

$$Q^*_e = \frac{m_e}{m_{single}} \tag{12}$$

$'m'_e$ and $'m'_{single}$ are the cumulative evaporated mass and pre-impacting droplet mass.

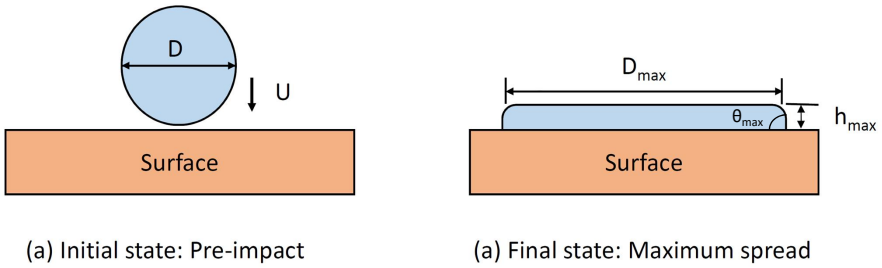

Figure 32: Single drop impact: Maximum spread

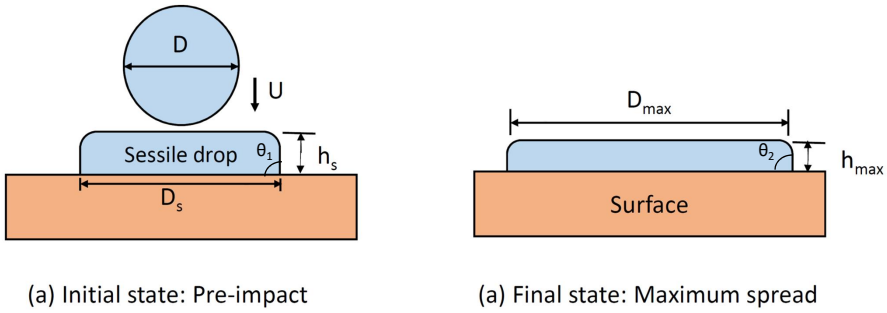

Figure 33: Drop-on-drop impact: Maximum Spread

A similar approach was applied to the drop-on-drop impingement over a hot surface by Guggilla et al.[53] as shown in Figure 33. In this case, the maximum spread factor is derived as

$$AS_{max}^{*\,5} + BS_{max}^{*\,3} + CS_{max}^{*} + D = 0 \tag{13}$$

where

$$A = \frac{18}{4} a \frac{We}{Re} \frac{1}{(1+c^3)(1-Q_e^*)} \tag{14}$$

$$B = 3(1-\cos\theta_2) \tag{15}$$

$$C = -(We + 4Bo + \frac{16c^3 Bo}{3S_{in}^{*\,2}} + 3S_{in}^{*\,2}(1-\cos\theta_1) + \frac{8c^3}{S_{in}^*} + 12) \tag{16}$$

$$D = 8(1+c^3)(1-Q_e^*) \tag{17}$$

and

$$\text{Bond number, Bo} = \frac{\rho_l g D^2}{4\sigma_{lv}} \tag{18}$$

$$\text{Reynolds number, Re} = \frac{\rho_l D U}{\mu} \tag{19}$$

$$\text{Weber number, We} = \frac{\rho_l D U^2}{\sigma_{lv}} \tag{20}$$

$$\text{Maximum spread factor, } S^*_{max} = \frac{D_{max}}{D} \tag{21}$$

$$\text{Initial spread factor, } S^*_{in} = \frac{D_s}{D} \tag{22}$$

Where, θ_1 and θ_2 are the corresponding contact angles at the initial and final states. Here constant $'a'$ is taken as 15, in order to approximate the present experimental observations, and $'c'$ is the radius ratio of impacting to sessile droplet (c = 1). In the present work, the liquid used is deionized water which is non-volatile and for the surface temperatures used, the total evaporation time of droplet is ranging from 720 seconds (at 50 ° C) to 100 seconds (at 175 ° C). The time interval between the two consecutive droplets at the considered flow rate of 20 droplets per minute (DPM) is around 3 seconds, and the total evaporated mass during this time is assumed to be negligible for the sessile droplet (equal volume as the impacting droplet) in the analytical model given in Equation 13. The evaporated mass during the impingement is calculated from the side view images of the droplet, and is used in Equations 11 and 17 to estimate the maximum spread factor.

It should be noted that the above correlations are able to capture the effects of all influential dimensionless parameters such as Weber number (We), Reynolds number (Re) and Bond number (Bo). The surface temperature effects are also considered in the form of evaporated mass (Q^*_e) and obtained contact angles (θ_1, θ_2) at respective temperatures. The present impingement scenario corresponds to an impact condition with We = 50, Bo = 0.27; and Re = 3180. The theoretical maximum spread factor at different temperatures are calculated using Equations 11 and 13 for single droplet and drop-on-drop impact respectively. The computed results are compared against experimental values as shown in Figure 34. The implemented theoretical models are found to be efficient in capturing the maximum spread values, and agreed well with experimental values within a deviation of 8% at all temperatures.

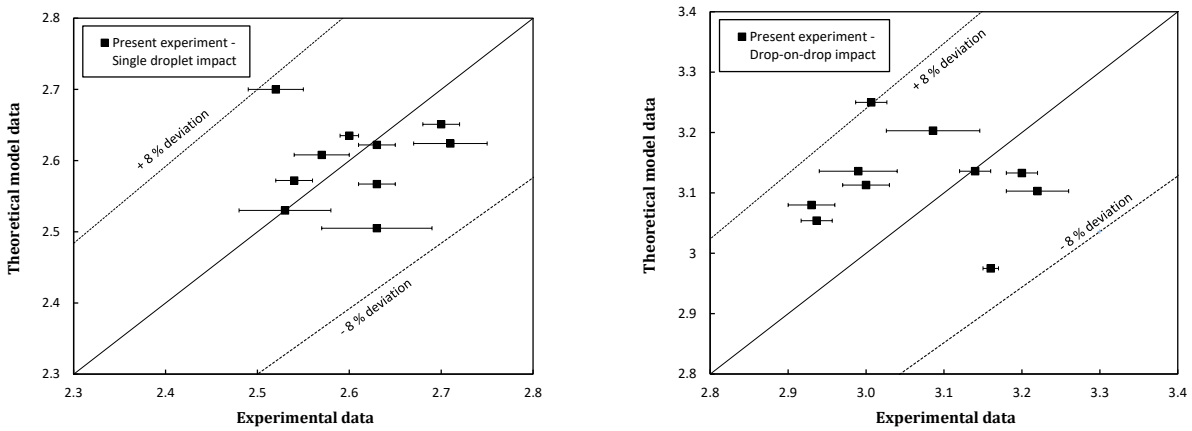

(a) Single droplet impingement

(b) Drop-on-drop impingement

Figure 34: Maximum spread factor: Experimental versus theoretical

4.4.2. Input heat transfer

It is evident that the bulk of heat transfer takes place during the spreading phase, and is accompanied by convection heat transfer, which can be modelled using a Nusselt number correlation. Assuming the spreading droplet as a single impinging jet, Batzdorf et al.[61] developed a theoretical model for estimating the overall heat transferred during the spreading phase which is proportional to the convective heat transfer, and is reproduced below.

$$Q^* = 3b\frac{S^*_{max}(S^*_{max}-1.1)}{(S^*_{max}-0.6)}\frac{(1+0.005Re^{0.55})^{0.5}Ja}{Re^{0.5}Pr^{0.58}}\tau_{max} \tag{23}$$

Here, Q^* is the effectiveness which is represented as

$$Q^* = \frac{\int_0^t (Q_{drop})dt}{mh_{lv}} \tag{24}$$

where all relevant properties are calculated at the film temperature, and the constant $'b'$ is taken as 0.1 in order to fit the experimental data.

The above correlation was used for estimating the heat transfer during single and drop-on-drop impact over the hot surface. The maximum spread factor S^*_{max} and the corresponding non-dimensional time τ_{max} during the initial cycle which is of order $\tau_{max} \sim 2$ (t = 5 ms) for single droplet impingement and $\tau_{max} \sim 3$ (t = 7.5 ms) for drop-on-drop impact, are taken from the experimental observations. Nonetheless, for drop-on-drop impingement, it is found that the effective heat transfer takes place in the annulus region of the initial and post-impact

droplet spread, as shown in Figure 31 (b). Hence, to obtain an accurate estimation of heat transfer, the *net spread factor* is more relevant and used in the Equation 23. Whereas for the single droplet impact, the spread factor and the corresponding time values are used. The

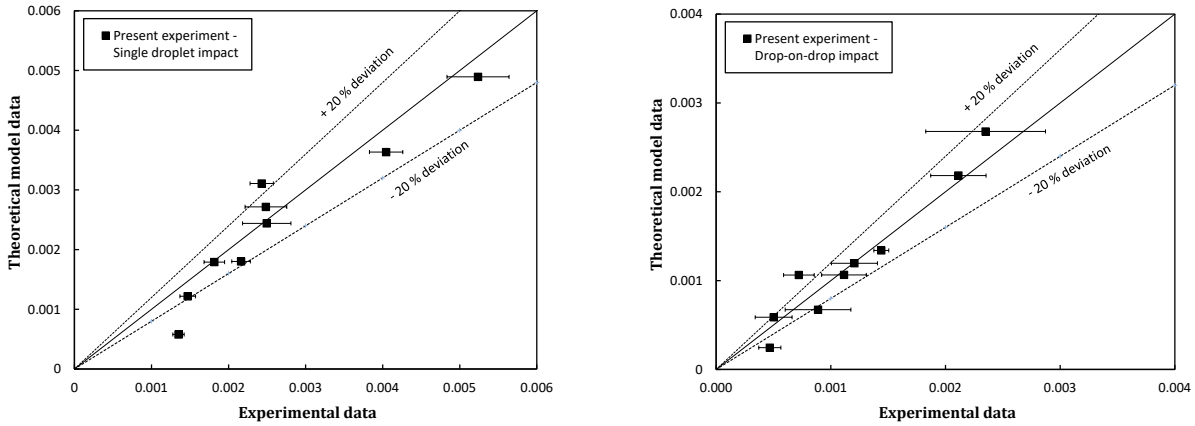

(a) Single droplet impingement

(b) Drop-on-drop impingement

Figure 35: Effectiveness: Experimental versus theoretical

theoretical results obtained is found to agree well with the experimental findings as shown in Figure 35. Especially for the drop-on-drop impact, the model is able to capture the heat transfer rate efficiently using *net spread factor*. The maximum deviation in the results are about 20 % and can be considered as a good approximation for heat transfer calculations.

Previous studies concerning the droplet impact over the heated surfaces are considered to validate the proposed correlations and examine the sensitivity of the constants $'a'$ and $'b'$ described in the Equations 11, 13, and 23. Teodari et al. [62] carried out the thermographic analysis of interfacial heat transfer mechanisms on drop/wall interactions. Single droplets of water and ethanol and a heated stainless steel surface (25μm), are utilized. The study examined the effect of the surface temperature, liquid surface tension, and wettability on heat transfer processes during a single droplet impact. Jung et al.[60] conducted heat transfer analysis of droplet collision over superheated surfaces and detected a dynamic Leidenfrost point based on the droplet heat transfer. In this work, water droplet impingement is carried out over the superheated platinum-coated sapphire glass maintained at temperatures of 176 - 226 °C. The details of the impingement studies, used for the present validation, are summarized in Table 4. The maximum spread factor, and the corresponding effectiveness,

Table 4: Experimental details of the considered literature cases in the analysis

Reference	Liquid-Surface	We	Re	Surface temperature (°C)	a	b
Teodari et al.[62]	Water on stainless steel (hydrophilic)	22.8	1980	100	15	0.1
Teodari et al.[62]	Water on stainless steel (hydrophilic)	22.8	1980	60	15	0.1
Teodari et al.[62]	Water on coated stainless steel (superhydrophobic)	22.8	1980	100	15	0.1
Teodari et al.[62]	Ethanol on stainless steel (hydrophilic)	50	1221	60	15	0.1
Jung et al.[60]	Water on platinum coated sapphire	6.3	1130	176	1	1.4
Jung et al.[60]	Water on platinum coated sapphire	6.3	1130	206	1	1.4
Jung et al.[60]	Water on platinum coated sapphire	6.3	1130	221	1	1.4
Present experiment	Water on Inconel surface (hydrophilic)	50	3180	22 - 175	15	0.1

as per equation 24, is calculated using the data from references [60, 62] and compared with the theoretical values from Equations 11 and 23. The constants $'a'$ and $'b'$ are chosen such that the theoretical values fit well with the experimental outcomes.

Figures 36 (a) and (b) show the comparison of experimental observations with theoretical results of maximum spread factor and effectiveness, respectively. In the case of Teodari et al.[62], the experimental conditions (liquid on the heated hydrophilic surface) are similar to the present work. so, the values of the constants a = 15 and b = 0.1 are considered. With these values, the correlations predicted the outcomes for the cases of the water droplet on the stainless steel surface (hydrophilic and super-hydrophobic) within the acceptable range. On the contrary, significant deviations in the results, are observed during the case of ethanol droplet impact over the heated surface. On the other hand, for the cases of Jung et al. [60], the constants a = 1 and b = 1.4 are found to provide a better approximation for the experimental observations. While the model for the maximum spread factor under-predicts the results, the effectiveness is observed to be within 25 % deviation, as given in Figure 36. The discrepancy with the spread factor prediction is due to the boiling phenomena reported

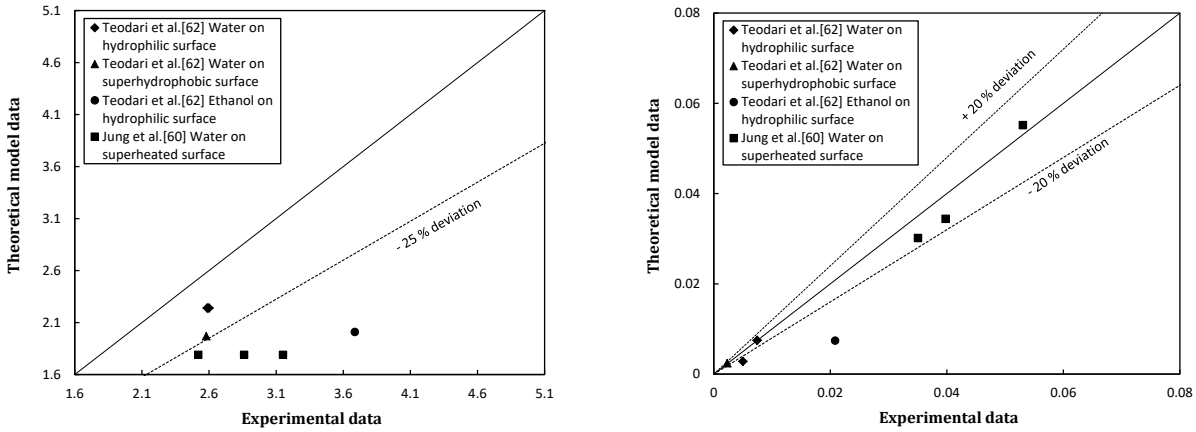

(a) Maximum spread factor

(b) Effectiveness

Figure 36: Validation: Experimental versus theoretical

in the droplet. And there is a need to account these effects, which are not included in the present model.

Moreover, in the previous studies of Batzdorf [61], the values a = 8/3 and b = 4/3, are adopted for FC-72 droplet collision over chromium surface and obtained a good approximation for the cases studied. Later on, Guggilla et al.[53] extended the study to drop-on-drop impact of FC-72 and the values of the same order, a = 8/3 and b = 3.4 are utilized to estimate the quantities. With these observations, it is determined that the analytical models are efficient in capturing the spread and heat transfer dynamics for the given constants $'a'$ and $'b'$, and these values are sensitive to the nature of the liquid, surface, and boiling regimes (wall superheat).

5. Summary and Conclusions

The present work provides results of an experimental investigation of the spread and heat transfer dynamics of a train of two concentric impinging droplets over a hot surface. At constant impact conditions (We = 50, Re = 3180), and flow rate of 20 droplets per minute (DPM), the behaviour is captured by high-speed imaging and infrared thermography. Deionized water droplets are impinged over the heated Inconel surface, and the surface temperature is chosen as a parameter, and varied from 22 °C (non-heated) to 175 °C. The impingement scenario is classified as single droplet and drop-on-drop configurations over the

hot surface and compared for relevant parameters. Outcomes such as spread factor, droplet input heat transfer, surface temperatures, effectiveness or cooling efficiency, and dynamic contact angle are obtained and compared. The following conclusions are made from the study.

1. The effect of temperature on spread dynamics is dominant from the initial cycle of spreading for both configurations. However, the maximum spread factor trends indicate that the spread factor is significantly affected by surface temperature during single droplet impingement compared to drop-on-drop impact.

2. High heat transfer rates are observed in the vicinity of the three-phase contact line, and input heat transfer rates are strongly influenced by the surface temperature during single droplet, as well as drop-on-drop impact over the surface.

3. Comparison of droplet input heat transfer between the configurations confirms that there is a reduction in the trailing droplet heat transfer, during drop-on-drop collision, compared to the leading droplet. The pre-cooling due to sessile droplet(initial) interaction and decrease in surface area-to-volume ratio is attributed to the low heat transfer rates observed during the drop-on-drop impact.

4. The extent of surface area being cooled has increased during drop-on-drop impingement, and the region corresponds to the *net spread factor* i.e., the annulus portion between the initial and post-impact spread is found to provide effective heat transfer during the impingement.

5. The dynamic contact angle variation is provided, for different surface temperatures, and the effect of temperature on contact angle is weak for both the configurations. Also, there is only a marginal increase of static contact angle over the heated surface due to the non-volatility of water.

6. To compare the input heat transfer rates among the configurations, an effectiveness ratio is defined as the ratio of dimensionless input heat transfer during drop-on-drop impact to a single droplet impingement. This parameter was found to be constant (around 0.62) for all surface temperatures concluding the reduction in heat transfer

during drop-on-drop impact.

7. Relevant analytical models available in literature were identified, and used to predict the maximum spread factor and heat transfer rates during the spreading phase for the present impingement configurations. The models captured the spread and heat transfer dynamics with a deviation of 8 % and 20 %, respectively. The performance of these models are examined with the previous studies for broader validity.

6. Appendix

6.1. Energy balance applied to a pixel element

The filtered temperature field is used and an energy balance is applied to each pixel to calculate the corresponding droplet heat transfer. The energy balance applied to the pixel element results in

$$Q_{stored} = Q_{gen} + Q_{cond} - Q_{rad} - Q_{conv} - Q_{drop} \tag{25}$$

where droplet input heat transfer is represented as Q_{drop}

Thus,

$$Q_{drop} = Q_{gen} - Q_{stored} + Q_{cond} - Q_{rad} - Q_{conv} \tag{26}$$

A continuous DC supply is provided to the surface and is maintained at a constant temperature. Upon droplet impingement, considerable heat transfer takes place resulting in the cooling of the surface. The generated heat due to the DC supply is calculated as Q_{gen}

$$Q_{gen} = \frac{I^2 R V_p}{V_s} \tag{27}$$

where I being the supplied current, V_p and V_s are the volumes of considered pixel element and total surface respectively.

Following the reference [56], the heater foil resistance 'R' is obtained from

$$R = \frac{\rho_s L_p (1 + \alpha_s (T - T_\infty))}{A_p} \tag{28}$$

where ρ_s, L_p , $A_p(= L_p\delta)$, α_s and δ represents surface electrical resistivity, pixel length, cross-sectional area, temperature coefficient of resistance, and thickness of the pixel element respectively. The properties of the surface is outlined in Table 2.

The net energy change in the pixel, is termed as stored heat Q_{stored}

$$Q_{stored} = \frac{m_s c(T_t - T_{t-1})}{dt} \tag{29}$$

where m_s is the mass of the pixel element, c specific heat capacity, T_t and T_{t-1} are the temperatures of the pixel element at a time intervals of t and $t-1$ respectively.

Due to negligible thickness [56, 62], the conduction effects perpendicular to the heater surface is minimal compared to other directions.

Thus, the conduction heat transfer along the surface is taken into account and is given as

$$Q_{cond} = (Q_{cond})_{in} - (Q_{cond})_{out} \tag{30}$$

can be simplified into

$$Q_{cond} = \frac{k_s A_p(T_{i+1,j} + T_{i-1,j} + T_{i,j+1} + T_{i,j-1} - 4T_{i,j})}{L_p} \tag{31}$$

where k_s is surface thermal conductivity and $T_{i,j}$ represents the temperature of considered element, and $T_{i+1,j}$, $T_{i-1,j}$, $T_{i,j+1}$, $T_{i,j-1}$ are the temperatures of neighbouring pixel elements in respective directions.

The bottom side of heater surface is coated black and is maintained at high temperatures. The radiation heat transfer underneath the surface is considered as

$$Q_{rad} = \sigma \epsilon_r L_p^2 ({T_{i,j}}^4 - {T_\infty}^4) \tag{32}$$

Also, natural convection currents will form eventually underneath the hot surface which can be calculated as

$$Q_{conv} = h_i L_p^2 (T_{i,j} - T_\infty) \tag{33}$$

where natural convectional heat transfer coefficient at a pixel element, h_i can be taken from the correlation

$$h_i = 0.27 {Ra_i}^{0.25} \tag{34}$$

and Ra_i is the Rayleigh number and all the properties are considered at the film temperature T_f

$$T_f = \frac{T_{i,j} + T_\infty}{2} \tag{35}$$

References

[1] A. Prosperetti, H. N. Oguz, The impact of drops on liquid surfaces and the underwater noise of rain, Annual Review of Fluid Mechanics 25 (1) (1993) 577–602.

[2] M. Rein, Phenomena of liquid drop impact on solid and liquid surfaces, Fluid Dynamics Research 12 (2) (1993) 61 – 93.

[3] A. Yarin, Drop impact dynamics: Splashing, spreading, receding, bouncing, Annual Review of Fluid Mechanics 38 (1) (2006) 159–192.

[4] M. Marengo, C. Antonini, I. V. Roisman, C. Tropea, Drop collisions with simple and complex surfaces, Current Opinion in Colloid and Interface Science 16 (4) (2011) 292 – 302.

[5] A. Moreira, A. Moita, M. Panão, Advances and challenges in explaining fuel spray impingement: How much of single droplet impact research is useful?, Progress in Energy and Combustion Science 36 (5) (2010) 554 – 580.

[6] C. Josserand, S. Thoroddsen, Drop impact on a solid surface, Annual Review of Fluid Mechanics 48 (1) (2016) 365–391.

[7] G. Liang, I. Mudawar, Review of drop impact on heated walls, International Journal of Heat and Mass Transfer 106 (2017) 103 – 126.

[8] Y. S. Ko, S. H. Chung, An experiment on the breakup of impinging droplets on a hot surface, Experiments in Fluids 21 (2) (1996) 118–123.

[9] J. D. Naber, P. V. Farrell, Hydrodynamics of droplet impingement on a heated surface, in: SAE Technical Paper, SAE International, 1993.

[10] J. D. Bernardin, C. J. Stebbins, I. Mudawar, Mapping of impact and heat transfer regimes of water drops impinging on a polished surface, International Journal of Heat and Mass Transfer 40 (2) (1997) 247 – 267.

[11] J. D. Bernardin, C. J. Stebbins, I. Mudawar, Effects of surface roughness on water droplet impact history and heat transfer regimes, International Journal of Heat and Mass Transfer 40 (1) (1996) 73 – 88.

[12] A.-B. Wang, C.-H. Lin, C.-C. Cheng, Pattern analysis of a single droplet impinging onto a heated plate, Heat Transfer Asian Research 34 (8) (2005) 579–594.

[13] A.-B. Wang, C.-H. Lin, C.-C. Chen, The critical temperature of dry impact for tiny droplet impinging on a heated surface, Physics of Fluids 12 (6) (2000) 1622–1625.

[14] H. J. J. Staat, T. Tran, B. Geerdink, G. Riboux, C. Sun, J. M. Gordillo, D. Lohse, Phase diagram for droplet impact on superheated surfaces, Journal of Fluid Mechanics 779 (2015) R3.

[15] T. Tran, H. J. J. Staat, A. Prosperetti, C. Sun, D. Lohse, Drop impact on superheated surfaces, Phys. Rev. Lett. 108 (2012) 036101.

[16] M. A. V. Limbeek, M. Shirota, P. Sleutel, C. Sun, A. Prosperetti, D. Lohse, Vapour cooling of poorly conducting hot substrates increases the dynamic Leidenfrost temperature, International Journal of Heat and Mass Transfer 97 (2016) 101 – 109.

[17] M. Di Marzo, D. D. Evans, Evaporation of a water droplet deposited on a hot high thermal conductivity surface, Journal of Heat Transfer 111 (1) (1989) 210–213.

[18] M. D. Marzo, P. Tartarini, Y. Liao, D. Evans, H. Baum, Evaporative cooling due to a gently deposited droplet, International Journal of Heat and Mass Transfer 36 (17) (1993) 4133 – 4139.

[19] O. E. Ruiz, W. Z. Black, Evaporation of water droplets placed on a heated horizontal surface, Journal of heat transfer 124 (5) (2002) 854–863.

[20] E. Berberović, I. V. Roisman, S. Jakirlić, C. Tropea, Inertia dominated flow and heat transfer in liquid drop spreading on a hot substrate, International Journal of Heat and Fluid Flow 32 (4) (2011) 785 – 795.

[21] G. Strotos, M. Gavaises, A. Theodorakakos, G. Bergeles, Numerical investigation on the evaporation of droplets depositing on heated surfaces at low Weber numbers, International Journal of Heat and Mass Transfer 51 (7) (2008) 1516 – 1529.

[22] S. Chandra, M. di Marzo, Y. Qiao, P. Tartarini, Effect of liquid-solid contact angle on droplet evaporation, Fire Safety Journal 27 (2) (1996) 141 – 158.

[23] M. Pasandideh-Fard, S. Aziz, S. Chandra, J. Mostaghimi, Cooling effectiveness of a water drop impinging on a hot surface, International Journal of Heat and Fluid Flow 22 (2) (2001) 201 – 210.

[24] Q. Cui, S. Chandra, S. McCahan, The effect of dissolving gases or solids in water droplets boiling on a hot surface, Journal of heat transfer 123 (4) (2001) 719–728.

[25] V. Nakoryakov, S. Misyura, S. Elistratov, The behavior of water droplets on the heated surface, International Journal of Heat and Mass Transfer 55 (23) (2012) 6609 – 6617.

[26] S. Herbert, T. Gambaryan-Roisman, P. Stephan, Influence of the governing dimensionless parameters on heat transfer during single drop impingement onto a hot wall, Colloids and Surfaces A: Physicochemical and Engineering Aspects 432 (2013) 57 – 63.

[27] M. Francois, W. Shyy, Computations of drop dynamics with the immersed boundary method, part 2: Drop impact and heat transfer, Numerical Heat Transfer, Part B: Fundamentals 44 (2) (2003) 119–143.

[28] G. Strotos, M. Gavaises, A. Theodorakakos, G. Bergeles, Numerical investigation of the cooling effectiveness of a droplet impinging on a heated surface, International Journal of Heat and Mass Transfer 51 (19) (2008) 4728 – 4742.

[29] Y. Ge, L.-S. Fan, 3-d modeling of the dynamics and heat transfer characteristics of subcooled droplet impact on a surface with film boiling, International Journal of Heat and Mass Transfer 49 (21) (2006) 4231 – 4249.

[30] W. Healy, J. Hartley, S. Abdel-Khalik, On the validity of the adiabatic spreading assumption in droplet impact cooling, International Journal of Heat and Mass Transfer 44 (20) (2001) 3869 – 3881.

[31] L. Tarozzi, A. Muscio, P. Tartarini, Experimental tests of dropwise cooling on infrared-transparent media, Experimental Thermal and Fluid Science 31 (8) (2007) 857 – 865.

[32] Y. M. Qiao, S. Chandra, Experiments on adding a surfactant to water drops boiling on a hot surface, Proceedings of the Royal Society of London. Series A: Mathematical, Physical and Engineering Sciences 453 (1959) (1997) 673–689.

[33] T. Okawa, K. Nagano, T. Hirano, Boiling heat transfer during single nanofluid drop impacts onto a hot wall, Experimental Thermal and Fluid Science 36 (2012) 78 – 85.

[34] T. Xiong, M. Yuen, Evaporation of a liquid droplet on a hot plate, International Journal of Heat and Mass Transfer 34 (7) (1991) 1881 – 1894.

[35] S. Kandlikar, M. Steinke, High speed photographic investigation of liquid-vapor interface and contact line movement during CHF and transition boiling, Vol. 369, 2001, pp. 323–329.

[36] F. McGinnis, J. Holman, Individual droplet heat-transfer rates for splattering on hot surfaces, International Journal of Heat and Mass Transfer 12 (1) (1969) 95 – 108.

[37] J. Holman, P. Jenkins, F. Sullivan, Experiments on individual droplet heat transfer rates, International Journal of Heat and Mass Transfer 15 (8) (1972) 1489 – 1495.

[38] J. Bernardin, I. Mudawar, The Leidenfrost point: experimental study and assessment of existing models, Journal of Heat Transfer 121 (4) (1999) 894–903.

[39] J. D. Bernardin, I. Mudawar, A cavity activation and bubble growth model of the leidenfrost point, Journal of Heat Transfer 124 (5) (2002) 864–874.

[40] C. Avedisian, J. Koplik, Leidenfrost boiling of methanol droplets on hot porous/ceramic surfaces, International Journal of Heat and Mass Transfer 30 (2) (1987) 379 – 393.

[41] C. Pedersen, An experimental study of the dynamic behavior and heat transfer characteristics of water droplets impinging upon a heated surface, International Journal of Heat and Mass Transfer 13 (2) (1970) 369 – 381.

[42] F. Celestini, T. Frisch, Y. Pomeau, Room temperature water Leidenfrost droplets, Soft Matter 9 (2013) 9535–9538.

[43] H.-m. Kwon, J. C. Bird, K. K. Varanasi, Increasing Leidenfrost point using micro-nano hierarchical surface structures, Applied Physics Letters 103 (20) (2013) 201601.

[44] D. Arnaldo del Cerro, l. G. Marín, G. R. B. E. Römer, B. Pathiraj, D. Lohse, A. J. Huis in 't Veld, Leidenfrost point reduction on micropatterned metallic surfaces, Langmuir 28 (42) (2012) 15106–15110.

[45] G. P. Celata, M. Cumo, A. Mariani, G. Zummo, Visualization of the impact of water drops on a hot surface: effect of drop velocity and surface inclination, Heat and Mass Transfer 42 (10) (2006) 885.

[46] V. Bertola, K. Sefiane, Controlling secondary atomization during drop impact on hot surfaces by polymer additives, Physics of Fluids 17 (10) (2005) 108104.

[47] D.V.Zaitsev, D. P. Kirichenko, V. S. Ajaev, O. A. Kabov, Levitation and self-organization of liquid microdroplets over dry heated substrates, Physical review letters 119 (9) (2017) 094503.

[48] O. A. Kabov, D. V. Zaitsev, D. P. Kirichenko, V. S. Ajaev, Interaction of levitating microdroplets with moist air flow in the contact line region, Nanoscale and microscale thermophysical engineering 21 (2) (2017) 60–69.

[49] J.D.Bernardin, I. Mudawar, film boiling heat transfer of droplet streams and sprays, International Journal of Heat and Mass Transfer 40 (11) (1997) 2579–2593.

[50] H. Fujimoto, A. Y. Tong, H. Takuda, Interaction phenomena of two water droplets successively impacting onto a solid surface, International Journal of Thermal Sciences 47 (3) (2008) 229 – 236.

[51] J. Breitenbach, I. V. Roisman, C. Tropea, From drop impact physics to spray cooling models: a critical review, Experiments in Fluids 59 (3) (2018) 55.

[52] T. Minamikawa, H. Fujimoto, T. Hama, H. Takuda, Numerical simulation of two droplets impinging successively on a hot solid in the film boiling regime, ISIJ International 48 (5) (2008) 611–615.

[53] G. Guggilla, A. Pattamatta, R. Narayanaswamy, Numerical investigation into the evaporation dynamics of drop-on-drop collisions over heated wetting surfaces, International Journal of Heat and Mass Transfer 123 (2018) 1050 – 1067.

[54] S. Batzdorf, J. Breitenbach, C. Schlawitschek, I. V. Roisman, C. Tropea, P. Stephan, T. Gambaryan-Roisman, Heat transfer during simultaneous impact of two drops onto a hot solid substrate, International Journal of Heat and Mass Transfer 113 (2017) 898 – 907.

[55] C. A. Schneider, W. S. Rasband, K. W. Eliceiri, NIH image to imagej: 25 years of image analysis, Nature methods 9 (7) (2012) 671.

[56] N. Schweizer, Multi-scale investigation of nucleate boiling phenomena in microgravity, Ph.D. thesis, Technische Universität, Darmstadt (2010).

[57] Š. Šikalo, H.-D. Wilhelm, I. Roisman, S. Jakirlić, C. Tropea, Dynamic contact angle of spreading droplets: Experiments and simulations, Physics of Fluids 17 (6) (2005) 062103.

[58] S. Chandra, C. Avedisian, On the collision of a droplet with a solid surface, Proc. R. Soc. Lond. A 432 (1884) (1991) 13–41.

[59] J. Wakefield, C. F. Tilger, M. A. Oehlschlaeger, The interaction of falling and sessile drops on a hydrophobic surface, Experimental Thermal and Fluid Science 79 (2016) 36–43.

[60] J. Jung, S. Jeong, H. Kim, Investigation of single-droplet/wall collision heat transfer characteristics using infrared thermometry, International Journal of Heat and Mass Transfer 92 (2016) 774–783.

[61] S. Batzdorf, Heat transfer and evaporation during single drop impingement onto a superheated wall, Ph.D. thesis, Technische Universität (2015).

[62] E.Teodori, P. Pontes, A. Moita, A. Moreira, Thermographic analysis of interfacial heat transfer mechanisms on droplet/wall interactions with high temporal and spatial resolution, Experimental Thermal and Fluid Science 96 (2018) 284–294.